Journal of Mathematical Biology (2021) 83:23
https://doi.org/10.1007/s00285-021-01641-y

Mathematical Biology

Invasive behaviour under competition via a free boundary model: a numerical approach

Kamruzzaman Khan[1,3] · Shuang Liu[2] · Timothy M. Schaerf[1] · Yihong Du[1]

Received: 16 June 2020 / Revised: 3 April 2021 / Accepted: 18 July 2021 /
Published online: 5 August 2021

Abstract

What will happen when two invasive species are competing and invading the environment at the same time? In this paper, we try to find all the possible scenarios in such a situation based on the diffusive Lotka-Volterra competition system with free boundaries. In a recent work, Du and Wu (Calc Var Partial Differ Equ, 57(2):52, 2018) considered a weak-strong competition case of this model (with spherical symmetry) and theoretically proved the existence of a "chase-and-run coexistence" phenomenon, for certain parameter ranges when the initial functions are chosen properly. Here we use a numerical approach to extend the theoretical research of Du and Wu (Calc Var Partial Differ Equ, 57(2):52, 2018) in several directions. Firstly, we examine how the longtime dynamics of the model changes as the initial functions are varied, and the simulation results suggest that there are four possible longtime profiles of the dynamics, with the chase-and-run coexistence the only possible profile when both species invade successfully. Secondly, we show through numerical experiments that the basic features of the model appear to be retained when the environment is perturbed by periodic variation in time. Thirdly, our numerical analysis suggests that in two space dimensions the population range and the spatial population distribution of the successful invader tend to become more and more circular as time increases no matter what geometrical shape the initial population range possesses. Our numerical simulations cover the one space dimension case, and two space dimension case with or without spherical symmetry. The numerical methods here are based on that of Liu et al. (Mathematics, 6(5):72, 2018, Int J Comput Math, 97(5): 959–979, 2020). In the two space

This work was partially supported by the Australian Research Council.

✉ Yihong Du
ydu@une.edu.au

1 School of Science and Technology, University of New England, Armidale, NSW 2351, Australia

2 Department of Mathematics, University of South Carolina, Columbia, USA

3 Department of Mathematics, Pabna University of Science and Technology, Pabna 6600, Bangladesh

dimension case without radial symmetry, the level set method is used, while the front tracking method is used for the remaining cases. We hope the numerical observations in this paper can provide further insights to the biological invasion problem, and also to future theoretical investigations. More importantly, we hope the numerical analysis may reach more biologically oriented experts and inspire applications of some refined versions of the model tailored to specific real world biological invasion problems.

Keywords Diffusive competition model · Free boundary · Longtime dynamics · Invasive behaviour

Mathematics Subject Classification 35K51 · 92D25 · 65M22

1 Introduction

The ecological impacts of invasive species is a widespread concern. For example, invasive cane toads (*Rhinella marina*) in Australia impose great danger to the survival of many native species, and extensive research has been performed on the ecological interactions between the cane toads and native frogs in Australia (Shine 2014). To predict the long-term dynamical behaviour and impact of invasive species, mathematical modelling plays an important role. After the pioneering works of Fisher (1937) and Kolmogorov et al. (1937), diffusive equations have been widely used in invasion ecology to analyse the spreading behaviour of invasive species. For two competing species invading into unbounded space, the following Lotka-Volterra competition system has been widely used to understand their dynamical behaviour (see, for example, Okubo et al. 1989):

$$\begin{cases} u_t = d_1 \Delta u + u(a_1 - b_1 u - c_1 v), \ x \in \mathbb{R}^N, \ t > 0, \\ v_t = d_2 \Delta v + v(a_2 - b_2 v - c_2 u), \ x \in \mathbb{R}^N, \ t > 0, \end{cases} \tag{1.1}$$

where $u(x,t)$ and $v(x,t)$ denote the population densities of the two competing species at time t and spatial location x; the positive constants d_i, a_i, b_i and c_i $(i = 1, 2)$ are the diffusion rates, intrinsic growth rates, intra-specific competition rates, and inter-specific competition rates, respectively.

For mathematical analysis, the number of parameters in (1.1) can be reduced. By using the scalings

$$\hat{u}(x,t) := \frac{b_1}{a_1} u\left(\sqrt{\frac{d_2}{a_2}}x, \frac{t}{a_2}\right), \ \hat{v}(x,t) := \frac{b_2}{a_2} v\left(\sqrt{\frac{d_2}{a_2}}x, \frac{t}{a_2}\right),$$
$$D := \frac{d_1}{d_2}, \ \gamma := \frac{a_1}{a_2}, \ k := \frac{a_2 c_1}{a_1 b_2}, \ h := \frac{a_1 c_2}{a_2 b_1},$$

and then omitting the hat signs, system (1.1) can be rewritten into the following simpler form,

$$\begin{cases} u_t = D\Delta u + \gamma u(1-u-kv), & x \in \mathbb{R}^N,\ t > 0, \\ v_t = \Delta v + v(1-v-hu), & x \in \mathbb{R}^N,\ t > 0. \end{cases} \tag{1.2}$$

The system (1.2) has four constant equilibrium solutions $(u, v) = (0, 0), (1, 0), (0, 1)$ and (u^*, v^*), where $(u^*, v^*) = \left(\frac{1-k}{1-hk}, \frac{1-h}{1-hk}\right)$ is meaningful only when $(1-k)(1-h) > 0$. If the entire Euclidean space $\mathbb{R}^N$ in (1.2) is replaced by a bounded open domain, and zero Neumann (no-flux) boundary conditions are imposed at the boundary of this domain, then it is well known that the asymptotic behaviour of the solution of system (1.2) with initial functions $u(x, 0), v(x, 0) > 0$ can be classified into the following four cases (see, for example, de Mottoni 1979):

(i) If $0 < k < 1 < h$, then

$$\lim_{t\to\infty} \big(u(x,t), v(x,t)\big) = (1, 0).$$

(ii) If $0 < h < 1 < k$, then

$$\lim_{t\to\infty} \big(u(x,t), v(x,t)\big) = (0, 1).$$

(iii) If $0 < h, k < 1$, then

$$\lim_{t\to\infty} \big(u(x,t), v(x,t)\big) = (u^*, v^*).$$

(iv) If $h, k > 1$, then (depending on the initial condition)

$$\lim_{t\to\infty} \big(u(x,t), v(x,t)\big) = (1, 0) \text{ or } (0, 1) \text{ or } (u^*, v^*).$$

Cases (i) and (ii) are known as the weak-strong competition cases (u strong and v weak in case (i)). Case (iii) is called the weak competition case and case (iv) is referred to as the strong competition case.

To use (1.2) to describe the spreading behaviour, one typically assumes that the initial populations $u(x, 0)$ and $v(x, 0)$ are positive in a bounded region of $\mathbb{R}^N$, and then uses the diffusive system to see how the populations evolve as time t increases. In the weak-strong competition case, say in case (i), the evolution of $\big(u(x,t), v(x,t)\big)$ can often be explained by a traveling wave solution of the system with a certain speed $c > 0$. This speed c is usually interpreted as the invading speed of u (and retreating speed of v). The dynamics can be more complex though; see Girardin and Lam (2019) for a very recent study of this case in space dimension $N = 1$.

A shortcoming of (1.2) as a population model is that, although the initial population ranges may be assumed to be bounded regions in space, that is, both $\{x \in \mathbb{R}^N : u(x, 0) > 0\}$ and $\{x \in \mathbb{R}^N : v(x, 0) > 0\}$ are bounded sets, once $t > 0$, the population ranges $\{x \in \mathbb{R}^N : u(x, t) > 0\}$ and $\{x \in \mathbb{R}^N : v(x, t) > 0\}$ coincide

with $\mathbb{R}^N$. Therefore (1.2) does not provide information for the evolution of the range boundaries of the species. To address this problem, recently several diffusive systems with free boundaries have been proposed and used to describe the spreading behaviour; see, for example, Du and Lin (2014), Du et al. (2017), Du and Wu (2018), Guo and Wu (2012, 2015), Tian and Ruan (2018), Wang and Zhang (2017), Wang et al. (2019), Wu (2013, 2015) for the case of two interacting competing species. The inclusion of free boundaries has significantly increased the level of difficulty to treat these already very challenging models with rich dynamics.

In this paper, we will start by focusing on the competition system with free boundaries in a radially symmetric setting considered in Du and Wu (2018), Guo and Wu (2015), which has the form (together with several other equations to be described below)

$$\begin{cases} u_t = D\Delta_r u + \gamma u(1-u-kv) & \text{for } 0 < r < s_1(t),\ t > 0, \\ v_t = \Delta_r v + v(1-v-hu) & \text{for } 0 < r < s_2(t),\ t > 0, \end{cases} \tag{1.3}$$

where $u(r,t)$ and $v(r,t)$ represent the population densities of the two competing species at spatial location $r(=|x|)$ and time t, and $\Delta_r\phi := \phi_{rr} + \frac{(N-1)}{r}\phi_r$ is the usual Laplacian operator in spherical coordinates with radial symmetry in $\mathbb{R}^N$. We will also consider some more general versions of (1.3), including the non-radial case in two space dimension, and cases of time-periodic environment.

In (1.3), the population range of u at time t is the ball $\{r < s_1(t)\}$ and that for v is the ball $\{r < s_2(t)\}$. The populations are assumed zero on and outside their range boundaries, namely

$$\begin{cases} u(r,t) \equiv 0 \ \text{ for } \ r \geq s_1(t) \ \text{ and } \ t > 0, \\ v(r,t) \equiv 0 \ \text{ for } \ r \geq s_2(t) \ \text{ and } \ t > 0. \end{cases} \tag{1.4}$$

Since the solutions are assumed spherically symmetric, at $r = 0$, the following conditions must hold:

$$u_r(0,t) = v_r(0,t) = 0 \text{ for } t > 0. \tag{1.5}$$

For the problem to be well-posed, equations governing the evolution of $s_1(t)$ and $s_2(t)$, as well as associated initial conditions, should be supplied. Following Du and Lin (2010), the following Stefan type conditions are used for $s_1(t)$ and $s_2(t)$ (see Bunting et al. (2012) for an interpretation based on ecological assumptions):

$$\begin{cases} s_1'(t) = -\mu_1 u_r(s_1(t),t) \text{ for } t > 0, \\ s_2'(t) = -\mu_2 v_r(s_2(t),t) \text{ for } t > 0, \end{cases} \tag{1.6}$$

where μ_1 and μ_2 are positive constants measuring the intention to spread into new territories of the species u and v respectively. The spheres $\{r = s_i(t)\}$, $i = 1, 2$, are known as free boundaries, which are part of the unknowns in the question, and the equations in (1.6) are called the free boundary conditions.

The initial conditions are

$$s_1(0) = s_1^0,\ s_2(0) = s_2^0,\ u(r,0) = u_0(r),\ v(r,0) = v_0(r)\ \text{ for }\ r \in [0,\infty), \quad (1.7)$$

where

$$\begin{cases} s_1^0 > 0 \text{ and } s_2^0 > 0, \\ u_0 \in C^2([0, s_1^0]) \text{ and } v_0 \in C^2([0, s_2^0]),\ u_0'(0) = v_0'(0) = 0, \\ u_0(r) > 0 \text{ for } r \in [0, s_1^0),\ u_0(r) = 0 \text{ for } r \geq s_1^0, \\ v_0(r) > 0 \text{ for } r \in [0, s_2^0),\ v_0(r) = 0 \text{ for } r \geq s_2^0. \end{cases} \quad (1.8)$$

It is known from Du and Wu (2018) that the equations (1.3) through to (1.7) always have a unique solution

$$(u, v, s_1, s_2) = (u(r,t), v(r,t), s_1(t), s_2(t)),$$

which is defined for all $t > 0$. Moreover, the long-time behaviour of the solution (u, v, s_1, s_2) is examined theoretically in Du and Wu (2018) for the weak-strong competition case

$$0 < k < 1 < h,$$

namely u and v are the strong and weak competitors, respectively.

The purpose of this paper is to numerically investigate this weak-strong competition case of (1.3)-(1.7) in several directions which are difficult to treat theoretically, and therefore not covered by Du and Wu (2018).

Let us now describe what has been obtained in Du and Wu (2018) and what we would like to gain through a numerical approach in this paper. We need to introduce two key numbers $s^*_{\mu_2}$ and $c^*_{\mu_1}$ first. By Propositions 2.1 and 2.2 of Bunting et al. (2012) (see also Theorem 6.2 in Du and Lou (2015) for a more general result), the following problem

$$\begin{cases} q'' + sq' + q(1-q) = 0,\ q > 0 \text{ in } (-\infty, 0), \\ q(0) = 0,\ q(-\infty) = 1 \end{cases} \quad (1.9)$$

has a unique solution q_s for every $s \in (0,2)$, and for each $\mu_2 > 0$, there exists a unique $s = s^*_{\mu_2} \in (0,2)$ such that $q_s'(0) = -s/\mu_2$. The ecological meaning of $s^*_{\mu_2}$ is the following (see Du and Lin (2010)):

The asymptotic spreading speed of v is $s^*_{\mu_2}$ when its competitor u is absent.

The number $c^*_{\mu_1}$ is determined in Theorem 1.3 of Du et al. (2017). With D, γ, k, h, μ_1 as in (1.3)-(1.7), there exists a unique $c = c^*_{\mu_1} > 0$ such that the

following semi-wave problem

$$\begin{cases} cU' + DU'' + \gamma U(1 - U - kV) = 0, & -\infty < \xi < 0, \\ cV' + V'' + V(1 - V - hU) = 0, & -\infty < \xi < \infty, \\ U(-\infty) = 1,\ U(0) = 0,\ U'(\xi) < 0 = U(-\xi),\ \xi < 0, \\ V(-\infty) = 0,\ V(+\infty) = 1,\ V'(\xi) > 0, & \xi \in \mathbb{R}, \end{cases} \tag{1.10}$$

has a unique solution (U_c, V_c) satisfying $c = \mu_1 U_c'(0)$. The ecological meaning of $c^*_{\mu_1}$ is (see Du et al. (2017)):

If the competitor v is a well-established native species in the model [1], *then u may invade into the territory of v with speed $c^*_{\mu_1}$.*

Du and Wu (2018) find that the long-time dynamical behaviour of (1.3)-(1.7) are strikingly different between the cases $c^*_{\mu_1} < s^*_{\mu_2}$ and $c^*_{\mu_1} > s^*_{\mu_2}$. In the latter case, at least one species will fail to establish, and vanish in the long-run, but when $c^*_{\mu_1} < s^*_{\mu_2}$ holds, for certain initial functions u_0 and v_0, the two species can both establish and successfully spread in the long-run; moreover, the unique solution (u, v, s_1, s_2) satisfies (Du and Wu 2018)

$$\begin{cases} \lim_{t\to\infty} \frac{s_1(t)}{t} = c^*_{\mu_1}, \quad \lim_{t\to\infty} \frac{s_2(t)}{t} = s^*_{\mu_2}, \\ \lim_{t\to\infty} (u(r,t), v(r,t)) = (1, 0) \text{ uniformly for } r \in [0, (c^*_{\mu_1} - \epsilon)t], \\ \lim_{t\to\infty} v(r,t) = 1 \text{ uniformly for } r \in [(c^*_{\mu_1} + \epsilon)t, (s^*_{\mu_2} - \epsilon)t], \end{cases} \tag{1.11}$$

for every small $\epsilon > 0$.

The results described in (1.11) indicate that the population range of the stronger competitor u spreads at asymptotic speed $c^*_{\mu_1}$, while that of the weaker competitor v spreads with faster asymptotic speed $s^*_{\mu_2}$, and the population mass of u roughly concentrates on the expanding ball $\{r < c^*_{\mu_1} t\}$, while that for v concentrates on the expending spherical shall $\{c^*_{\mu_1} t < r < s^*_{\mu_2} t\}$ which shifts to infinity as $t \to \infty$. Note also that, apart from a relatively thin region near the sphere $\{r = c^*_{\mu_1} t\}$, the population masses of u and v are largely segregated for all large time. The phenomenon described by (1.11) may be interpreted by saying that the weak competitor v survives the competition from u by outrunning it with a faster speed. For this reason, we will refer to this phenomenon as **chase-and-run coexistence**.

While sufficient conditions on the initial functions u_0 and v_0 are given in Du and Wu (2018) for the above chase-and-run coexistence phenomenon, these conditions are rather restrictive, and one naturally wonders what would happen to the solution when these conditions are not satisfied. The first aim of this paper is to numerically investigate how the long-time dynamical behaviour of the model changes as the initial functions are varied. For this purpose, we consider initial functions u_0 and v_0 which vary continuously with some parameters, say $u_0 = u_0(r; \lambda_1)$, $v_0 = v_0(r; \lambda_2)$. We vary the parameters λ_1 and λ_2 in a suitable range, and examine numerically the solution

[1] Which means $s_2(t) \equiv \infty$ and $\inf_{r\geq 0} v(r, 0) > 0$. See Du et al. (2017) for precise statement.

of the model and demonstrate that, at least in the checked parameter ranges, the long-time dynamics can be classified into the following four cases, namely

$$\begin{cases} \text{(i) chase-and-run coexistence as described in (1.11)above,} \\ \text{(ii) vanishing of } u \text{ with } v \text{ invading successfully,} \\ \text{(iii) vanishing of } v \text{ with } u \text{ invading successfully,} \\ \text{(iv) vanishing of both } u \text{ and } v. \end{cases} \tag{1.12}$$

This is carried out in Sect. 2 below.

Secondly, we investigate what happens if in the model the homogeneous environment is changed to a time-periodic one, which is a natural situation since most species are affected by daily or seasonal changes of the natural world. Our numerical analysis indicates that the basic features of the model are retained under this change. The details are given in Sect. 3.

Thirdly, we numerically simulate the model when the spherical symmetry in the model is violated. For a single species model, such a non-spherical case was theoretically investigated in Du and Guo (2012), Du et al. (2014), and it was shown that the basic features of the long-time dynamical behaviour of the model are similar to the spherically symmetric case, and moreover, when spreading is successful, the population range becomes more and more like an enlarging ball as time increases. Here for the two species model, we demonstrate a similar phenomenon through numerical experiments. This is the content of Sect. 4 (see also Sect. 2.4).

Numerical treatment of related diffusive systems with free boundary conditions has been developed in several recent works; see, for example, Liu et al. (2020), Liu and Liu (2018), Liu and Liu (2020), Piqueras et al. (2017). These works mainly focus on the numerical techniques that can accurately simulate this type of free boundary problem, while our work here focuses on the long-time dynamical behaviours of a specific model. The numerical methods employed here are based on Liu et al. (2020), Liu and Liu (2018). More precisely, for the 1 space dimension case and the spherically symmetric case in 2 space dimension, we use the front tracking method, while for the non-symmetric case in 2 space dimension, the level set method is employed. We note that in order to observe the long time dynamical behaviour of our solutions here, time-consuming calculations are necessary, and to make our study tractable in a reasonable amount of CPU time, we have to modify the numerical methods in Liu et al. (2020), Liu and Liu (2018) to use explicit, rather than implicit, time integration (the implicit methods take much longer time for the same calculation). The details on the numerical methods used in this paper, as well as further explanations on the numerical experiments carried out here can be found in the Appendix of Khan et al. (2020), which is a fuller version of the current paper.

Needless to say, the numerical observations obtained in this paper are based on a particular way of choosing the initial functions, and should be interpreted with great care. For example, there could be borderline cases which are not picked up by the numerical experiments and therefore missing from the above listed cases (i)-(iv). It is also possible (though we believe it is unlikely) that by choosing the parametrised initial functions differently, different phenomena may occur. Nevertheless, we hope

the numerical observations in this paper can provide helpful insights to the biological problem as well as to future theoretical investigations.

2 Change of dynamical behaviour as the initial functions are varied

The purpose of this section is to use numerical simulations to find all possible long-time dynamical behaviour of the model, by varying the initial functions. Since it is impossible to exhaust all possible initial functions, in practice we will examine a parameterized family of initial functions $(u_0(.,\lambda_1), v_0(.,\lambda_2))$ with λ_1 and λ_2 the parameters. As will be seen below, we have the following observations from the numerical experiments.

Observation 1 *In the case $c^*_{\mu_1} < s^*_{\mu_2}$, depending on the initial states of the two species, there are four types of long-time behaviour of the system, as described in* (1.12).

2.1 The 1D case

In this subsection, we use the front tracking method similar to that described in Liu and Liu (2018), Liu et al. (2020) to simulate the evolution of the invasion modelled by (1.3)–(1.7) in one space dimension (1D), and confirm *Observation* 1 in this case.

We first choose the parameters in the model such that $0 < k < 1 < h$ and $c^*_{\mu_1} < s^*_{\mu_2}$. For $(D, h, k, \gamma, \mu_1, \mu_2) = (2, 2, 0.5, 2, 0.1, 1)$, it can be estimated from our simulations that[2]

$$c^*_{\mu_1} \approx 0.045094, \ \ s^*_{\mu_2} \approx 0.364366.$$

As for the initial functions, we take

$$u_0 = u_0(x, \lambda_1) \text{ and } v_0 = v_0(x, \lambda_2)$$

with

$$u_0(x,\lambda_1) = \begin{cases} 1, & \text{if } x \in [0, \frac{\lambda_1\pi}{2}] \\ \sin(x/\lambda_1), & \text{if } x \in [\frac{\lambda_1\pi}{2}, \lambda_1\pi] \end{cases} \tag{2.1}$$

$$v_0(x,\lambda_2) = \begin{cases} \sin(\epsilon), & \text{if } x \in [0, \epsilon\lambda_2] \\ \sin(x/\lambda_2), & \text{if } x \in [\epsilon\lambda_2, \lambda_2\pi] \end{cases} \tag{2.2}$$

where $\epsilon = \arcsin(0.1)$. The parameters λ_1 and λ_2 will be chosen from the interval $[0.1, 20]$. Correspondingly,

$$s^0_1 = \lambda_1\pi \text{ and } s^0_2 = \lambda_2\pi.$$

In our simulations, we firstly fix λ_1 to a value from the set {0.01, 0.05, 0.10, 0.15, 0.20, 0.25, 0.30, 0.35, 0.40, 0.45, 0.50, 0.55, 0.60, 0.65, 0.75, 0.85, 1, 1.5, 2, 2.5,

[2] Here we have used (1.11) to estimate $(c^*_{\mu_1}, s^*_{\mu_2})$ by $(s_1'(t), s_2'(t))$ for large enough t, with a suitably chosen initial function pair.

3, 4, 5, 6, 7} and then vary the values of λ_2 to see how the long-time dynamics of the model changes. We will call this group of simulations "type A test". This test ultimately shows that the long-time behavior of each of the four cases described in *Observation* 1 above can be detected, and only these four cases occur. We remark that near any critical value of λ_2 (with a fixed λ_1 in the set given above), a sequence of nearby values of λ_2 with very small spacing are used in the test.

We also run a "type B test", where the roles of λ_1 and λ_2 are largely reversed in the simulations, namely, we fix λ_2 to a value in the set {0.01, 0.05, 0.10, 0.15, 0.20, 0.25, 0.30, 0.32, 0.35, 0.40, 0.45, 0.50, 0.75, 1, 1.5, 2, 2.5, 3, 4, 5, 6, 7}, and then vary λ_1 to see how the long-time dynamics changes. Again all four types of behaviour described in *Observation* 1 can be detected, and only these four cases occur.

Numerical results from our type A and type B tests are summarized in Fig. 1, where the parameter region $(\lambda_1, \lambda_2) \in [0.01, 3] \times [0.01, 3]$ is divided into 4 subregions, with each region yielding a different long-time dynamical behavior of the model; for example, if (λ_1, λ_2) lies in the yellow region, then chase-and-run coexistence happens when the initial functions in (2.1) and (2.2) take this pair of (λ_1, λ_2) values. Figure 2 gives the precise set of values of (λ_1, λ_2) for which we have done the numerical simulations. The complete list of values of λ_1 and λ_2 used in our type A test and type B test, which are used to generate Fig. 1, and the approximate critical values where change of behavior occurs, are given in Tables 1 and 2 in the "Appendix" of Khan et al. (2020).

In these simulations, we set a priori a finite range $[0, \mathcal{L}]$ for the variable x, which is meshed into small intervals of size $\Delta x = \frac{\mathcal{L}}{\mathcal{N}_x}$. The time variable t is discretized accordingly with step size $\Delta t = \frac{0.1\times(\Delta x)^2}{D}$, where D is the diffusion rate in the model. $\mathcal{L}$ is chosen large enough so that the free boundaries $x = s_1(t)$ and $x = s_2(t)$ lie in the interval $[0, \mathcal{L}]$ for the time range under simulation. More precisely, in the simulations for Figs. 1 and 2, the parameters in the model are set as $(D, h, k, \gamma, \mu_1, \mu_2) = (2, 2, 0.5, 2, 0.1, 1)$, time step $\Delta t = 5 \times 10^{-6}$, space mesh size $\Delta x = 0.01$. The calculation for each choice of (λ_1, λ_2) is run until $t = 120$, well after the dynamical behavior of the solution stablizes.

Let us note that once we know which type of dynamical behavior occurs, the known theoretical results provide a rather precise description of this behavior. Indeed, if case (i) happens, we know that (1.11) holds for the solution $(u(x, t), v(x, t), s_1(t), s_2(t))$.

By Du et al. (2015a), if case (ii) happens, then there exist some constants C_1 and C_2 depending on the initial data, such that

$$\begin{cases} \lim_{t\to\infty} s_1(t) = C_1,\ \lim_{t\to\infty} \left[s_2(t) - s^*_{\mu_2} t\right] = C_2,\ \lim_{t\to\infty} s_2'(t) = s^*_{\mu_2}, \\ \lim_{t\to\infty} \max_{x\in[0,s_1(t)]} u(x, t) = 0, \\ \lim_{t\to\infty} \left\{ \max_{x\in[0,s_2(t)]} \left|v(x, t) - p_{s^*_{\mu_2}}(x - s_2(t))\right| \right\} = 0; \end{cases}$$

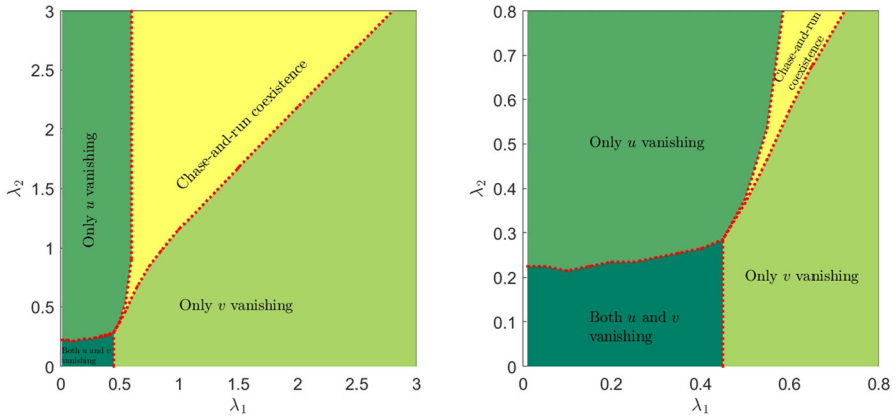

(A) $(\lambda_1, \lambda_2) \in [0.01, 3]^2$. **(B)** $(\lambda_1, \lambda_2) \in [0.01, 0.8]^2$.

Fig. 1 Change of longtime dynamical behavior in the 1D case as (λ_1, λ_2) varies. The red dotted lines represent the critical curves where the species change their longtime dynamical behavior as the point (λ_1, λ_2) crosses them (color figure online)

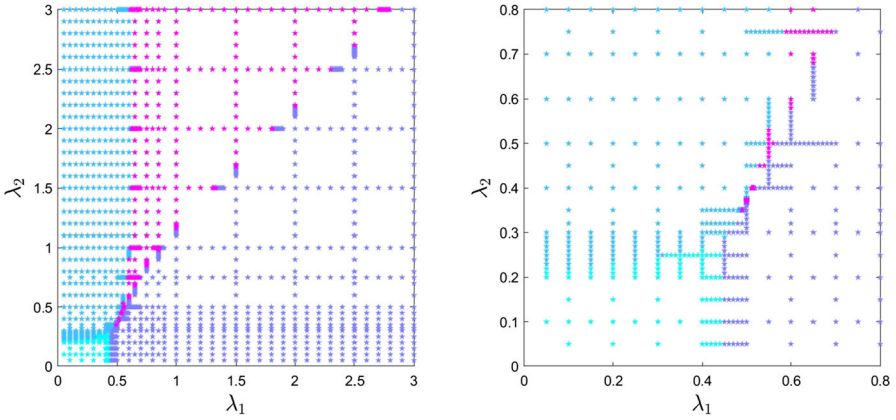

(A) $(\lambda_1, \lambda_2) \in [0.01, 3]^2$. **(B)** $(\lambda_1, \lambda_2) \in [0.01, 0.8]^2$.

Fig. 2 Points of (λ_1, λ_2) for which simulations are run to produce Fig. 1 are marked with stars

and if case (iii) happens, then there exist some constants $\tilde{C}_1$ and $\tilde{C}_2$ depending on the initial data, such that

$$\begin{cases} \lim_{t\to\infty} \left[s_1(t) - s^*_{\mu_1} t \right] = \tilde{C}_1, \ \lim_{t\to\infty} s_1'(t) = s^*_{\mu_1}, \ \lim_{t\to\infty} s_2(t) = \tilde{C}_2, \\ \lim_{t\to\infty} \left\{ \max_{x\in[0,s_1(t)]} \left| u(x,t) - q_{s^*_{\mu_1}}(x - s_1(t)) \right| \right\} = 0, \\ \lim_{t\to\infty} \max_{x\in[0,s_2(t)]} v(x,t) = 0, \end{cases}$$

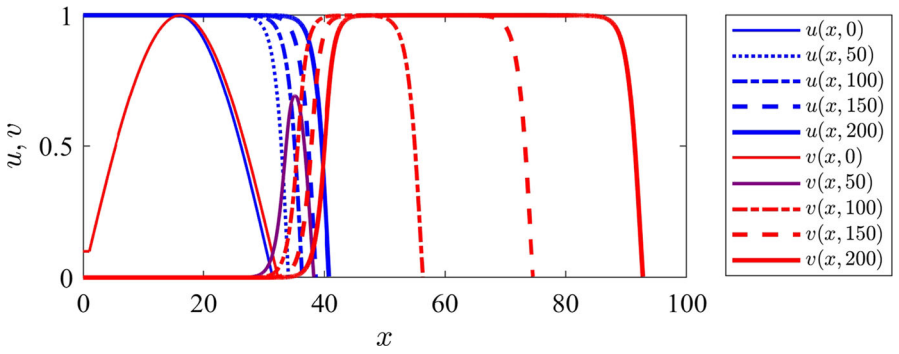

Fig. 3 Profiles of $u(x,t)$ (blue curves) and $v(x,t)$ (red curves) with $(\lambda_1, \lambda_2) = (10, 10.280)$ at time moments $t = 0, 50, 100, 150, 200$, showing clear traveling wave behaviour for large t (color figure online)

where the constant $s^*_{\mu_1} > 0$ and the positive function $q_{s^*_{\mu_1}}$ are determined by the following result of Bunting et al. (2012): *The problem*

$$\begin{cases} Dq'' + sq' + \gamma q(1-q) = 0, \ q > 0 \ \text{in } (-\infty, 0), \\ q(0) = 0, \ q(-\infty) = 1 \end{cases} \tag{2.3}$$

has a unique solution q_s for every $s \in (0, 2\sqrt{D\gamma})$, and for each $\mu_1 > 0$, there exists a unique $s = s^*_{\mu_1} \in (0, 2\sqrt{D\gamma})$ such that $q_s'(0) = -s/\mu_1$.

If case (iv) happens, then it follows from Du and Lin (2010) that there exist positive constants $\hat{C}_1$ and $\hat{C}_2$ depending on the initial data such that

$$\begin{cases} \lim_{t\to\infty} s_1(t) = \hat{C}_1, \ \lim_{t\to\infty} s_2(t) = \hat{C}_2, \\ \lim_{t\to\infty} \max_{x\in[0,s_1(t)]} u(x,t) = 0, \\ \lim_{t\to\infty} \max_{x\in[0,s_2(t)]} v(x,t) = 0. \end{cases}$$

A numerical sample for case (i) A sample of simulation results for case (i) (chase-and-run) is presented in Figs. 3 and 4, where snap-shots of the profiles of $u(x,t)$ and $v(x,t)$ are shown in Fig. 3 for the time moments: $t = 0, t = 50, t = 100, t = 150$, and $t = 200$. The curves $s_1(t)$ and $s_2(t)$ are shown in Fig. 4. In this sample, we have taken $\lambda_1 = 10, \ \lambda_2 = 10.280$, and the other parameters are the same as in the simulations for Figs. 1 and 2, except that now the calculation is run until $t = 200$.

A numerical sample for case (iii) The above sample is obtained with $(\lambda_1, \lambda_2) = (10, 10.280)$. If the λ_2 value is changed to $\lambda_2 = 10.279$, while all the other parameter values are unchanged, the longtime behavior changes from case (i) to case (iii). Our simulation results are presented in Figs. 5 and 6.

A numerical sample for case (ii) Figures 7 and 8 describe a situation for case (ii), obtained from numerical simulation for $\lambda_1 = 0.60, \ \lambda_2 = 0.95$, while all other parameters are the same as in the simulations for Figs. 1, 2, 3, 4, 5, 6.

A numerical sample for case (iv) Figures 9 and 10 are obtained from numerical simulation with $\lambda_1 = 0.40, \ \lambda_2 = 0.26$, while all other parameters are the same as

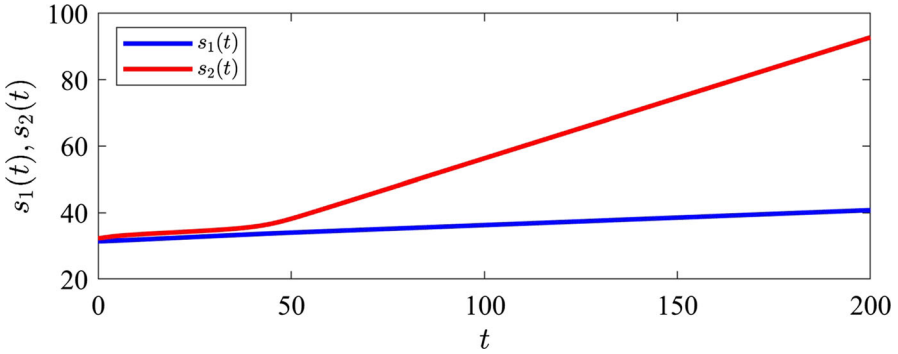

Fig. 4 Corresponding behaviour of $s_1(t)$ (blue curve) and $s_2(t)$ (red curve) in Fig. 3, showing eventual linear growth in time for both functions (color figure online)

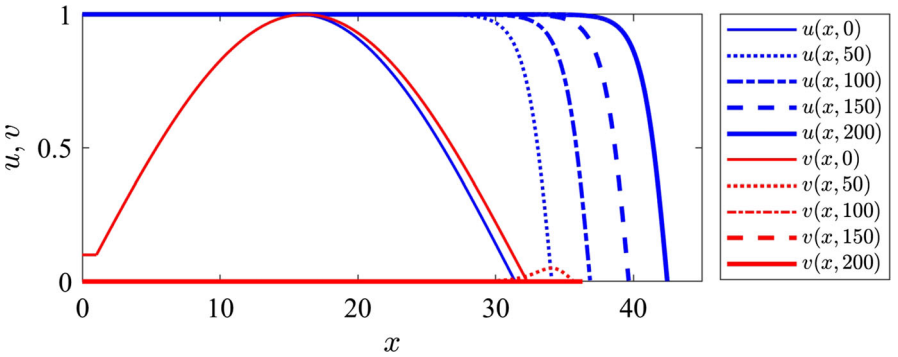

Fig. 5 Profiles of $u(x,t)$ (blue curve) and $v(x,t)$ (red curve) with $(\lambda_1, \lambda_2) = (10, 10.279)$ at time $t = 0, 50, 100, 150, 200$, showing the vanishing of v and the spreading of u like a traveling wave for large time (color figure online)

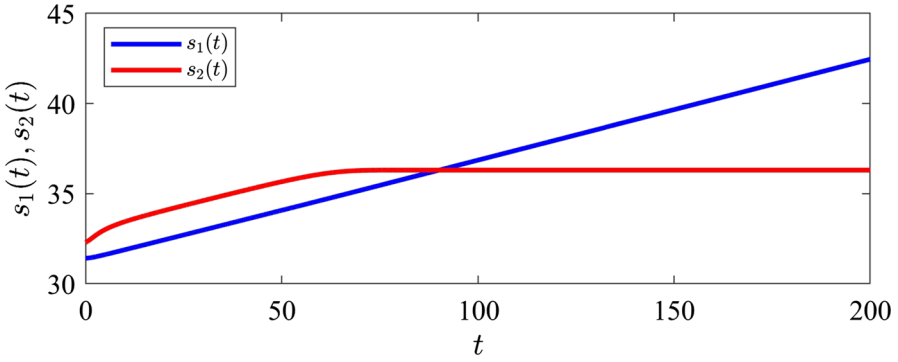

Fig. 6 Corresponding behaviour of $s_1(t)$ and $s_2(t)$ in Fig. 5, showing $s_2(t)$ converging to a finite value and $s_1(t)$ growing linearly in time

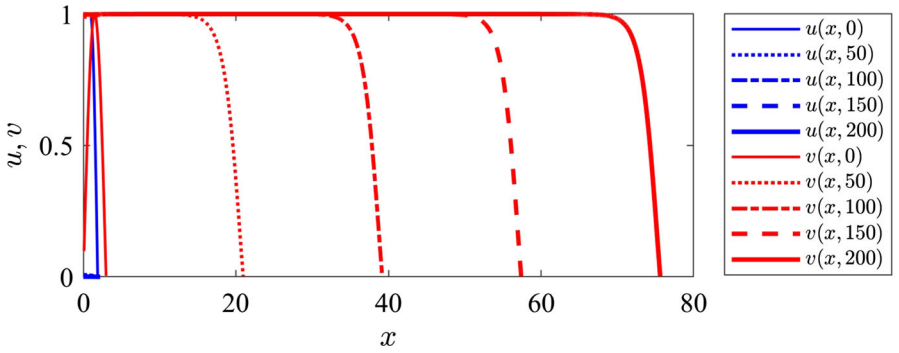

Fig. 7 Travelling wave profile of $v(x,t)$ (red curves) and extinction profile of $u(x,t)$ (blue curves) with $(\lambda_1, \lambda_2) = (0.60, 0.95)$ at time $t = 0, 50, 100, 150, 200$ (color figure online)

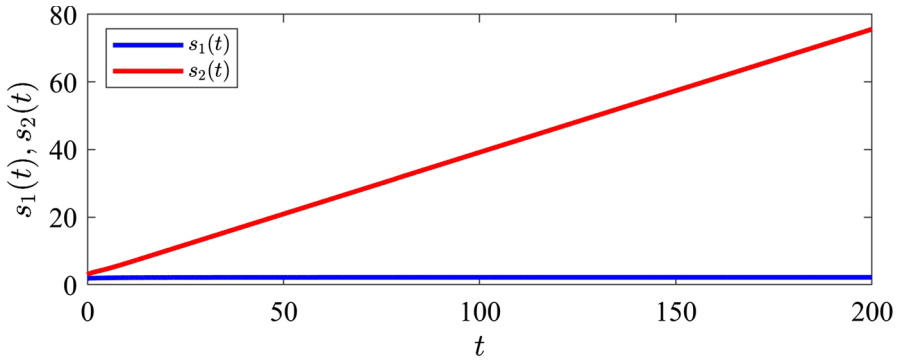

Fig. 8 Corresponding behaviour of $s_1(t)$ and $s_2(t)$ in Figure 7, showing $s_1(t)$ converging to a finite value and $s_2(t)$ growing linearly in time (color figure online)

in the simulations for Figs. 1, 2, 3, 4, 5, 6, 7, 8, showing both u and v vanishing eventually.

2.2 The 2D radially symmetric case

We now consider the model in 2 spatial dimensions with radial symmetry, and so we will write $r = \sqrt{x^2 + y^2}$ and denote the solution by $(u, v) \equiv (u(r,t), v(r,t))$.

The initial functions u_0 and v_0 used for our simulations are given by

$$u_0(r, \lambda_1) = \begin{cases} 1, & \text{if } r \in [0, \frac{\lambda_1 \pi}{2}], \\ \sin(r/\lambda_1), & \text{if } r \in [\frac{\lambda_1 \pi}{2}, \lambda_1 \pi], \end{cases} \tag{2.4}$$

$$v_0(r, \lambda_2) = \begin{cases} \sin \epsilon, & \text{if } r \in [0, \epsilon \lambda_2], \\ \sin(r/\lambda_2), & \text{if } r \in [\epsilon \lambda_2, \lambda_2 \pi], \end{cases} \tag{2.5}$$

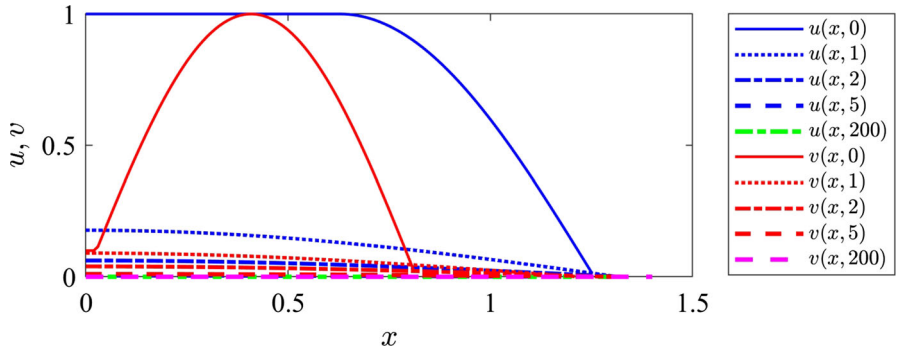

Fig. 9 Profiles of $u(x,t)$ (blue curve) and $v(x,t)$ (red curve) with $(\lambda_1, \lambda_2) = (0.40, 0.26)$ at time $t = 0, 50, 100, 150, 200$, showing the vanishing of both u and v for large time

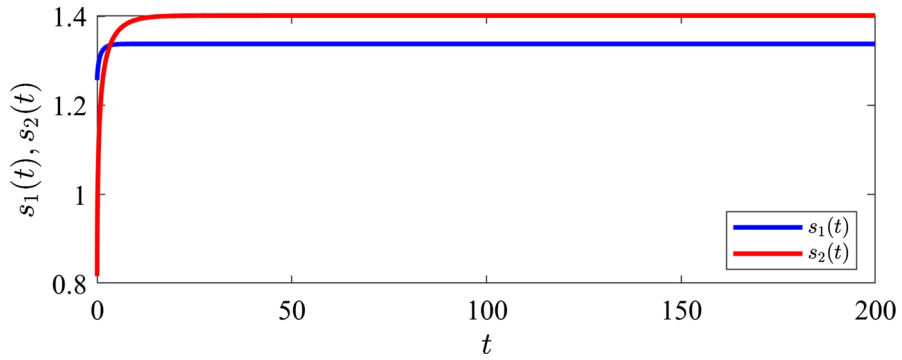

Fig. 10 Corresponding behaviour of $s_1(t)$ and $s_2(t)$ in Fig. 9

where $\epsilon = \arcsin(0.1)$. Accordingly, we have

$$s_1(0) = \lambda_1 \pi, \ s_2(0) = \lambda_2 \pi.$$

Due to the radial symmetry of the solutions, for the simulation, we could use either the front tracking method or the level set method as described in Liu and Liu (2018). Here we use the front tracking method, with $(D, h, k, \gamma, \mu_1, \mu_2) = (2, 2, 0.5, 2, 0.1, 1)$, time step $\Delta t = 5 \times 10^{-6}$, space mesh size $\Delta r = 0.01$, and the calculation is run until $t = 120$ or 200.

As in the previous subsection, we run both type A tests and type B tests, to check whether the statements in Observation 1 hold. Our numerical simulations again confirm what we expected. The details of the tested values of the parameters (λ_1, λ_2) from (2.4) and (2.5) are summerized in Tables 3 and 4 in "Appendix" B of Khan et al. (2020).

The figures parallel to those in the previous subsection arising from the simulation here are listed below (Fig. 11, 12, 13, 14, 15, 16, 17, 18, 19, 20).

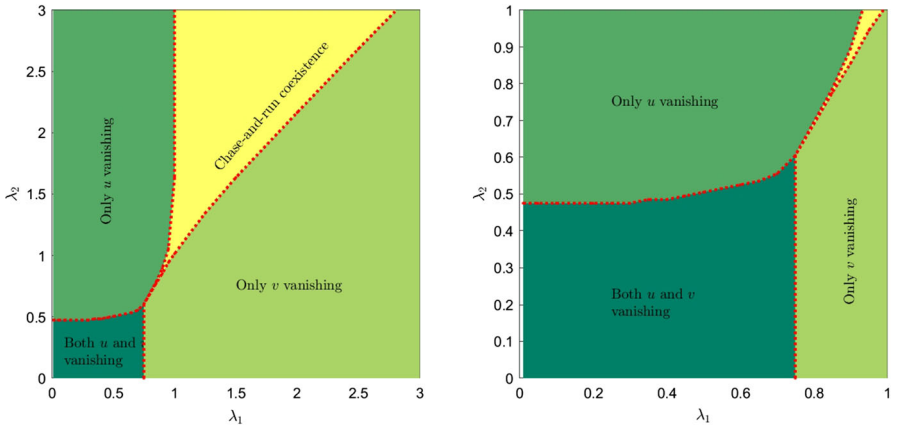

(A) $(\lambda_1, \lambda_2) \in [0.01, 3.0]^2$. **(B)** $(\lambda_1, \lambda_2) \in [0.01, 1.0]^2$.

Fig. 11 Change of longtime dynamical behavior in the 2D radial case as (λ_1, λ_2) varies. Model parameters $(D, h, k, \gamma, \mu_1, \mu_2) = (2, 2, 0.5, 2, 0.1, 1)$, time step $\Delta t = 5 \times 10^{-6}$, space step $\Delta r = 0.01$, and the calculation is run until $t = 120$

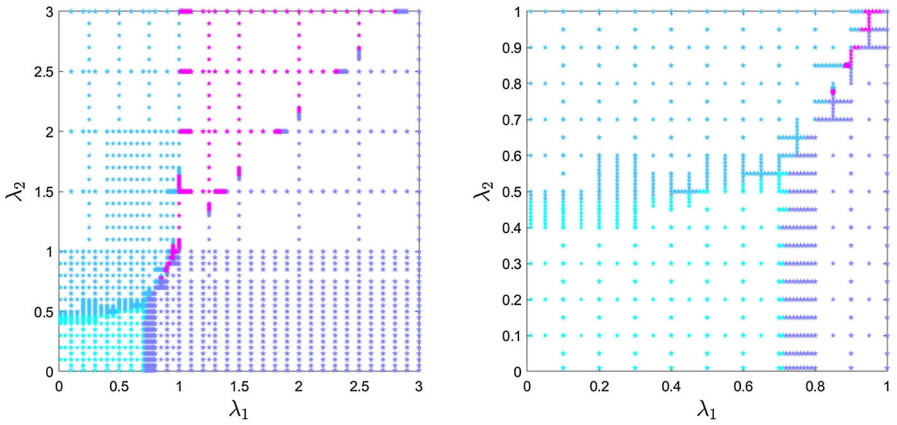

(A) $(\lambda_1, \lambda_2) \in [0.01, 3.0]^2$. **(B)** $(\lambda_1, \lambda_2) \in [0.01, 1.0]^2$.

Fig. 12 Points of (λ_1, λ_2) for which simulations are run to produce Fig. 11 are marked with stars

2.3 Comparison of the fronts in 1D and in 2D with radial symmetry

We would like to stress that existing theoretical results indicate that for the radially symmetric case in two space dimensions, the theoretical descriptions for cases (i)-(iv) in the previous subsection remain valid when x there is replaced by $r = |x|$, except that in case (ii), $\lim_{t\to\infty}[s_2(t) - s^*_{\mu_2} t] = C_2$ should be replaced by

$$\lim_{t\to\infty} \left\{ s_2(t) - \left[s^*_{\mu_2} t - c^*_2 \ln t \right] \right\} = C_2 \text{ for some } C_2 \in \mathbb{R}, \tag{2.6}$$

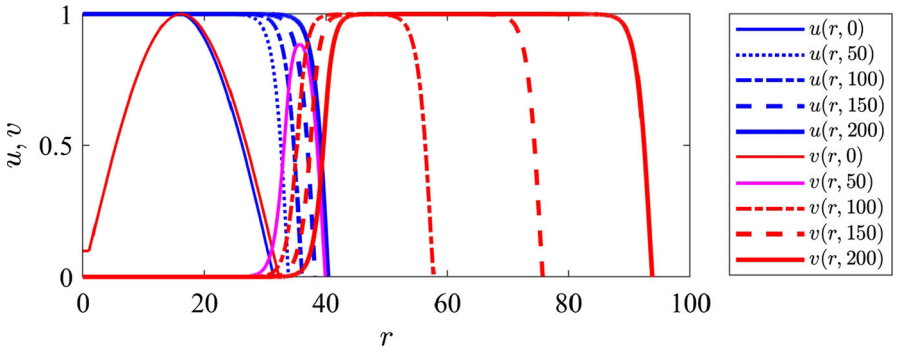

Fig. 13 Sample case (i) in 2D with radial symmetry. Profiles of $u(r, t)$ (blue curve) and $v(r, t)$ (red curve) with $(\lambda_1, \lambda_2) = (10, 10.28)$ at time $t = 0, 50, 100, 150, 200$, showing clear traveling wave behaviour for large t (color figure online)

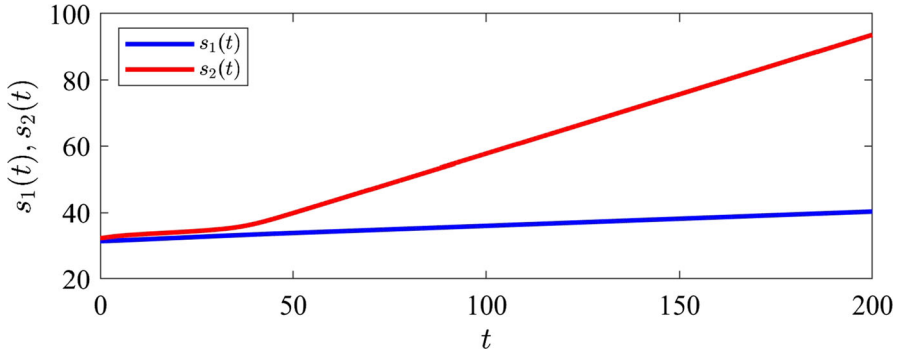

Fig. 14 Corresponding behaviour of $s_1(t)$ (blue curve) and $s_2(t)$ (red curve) in Fig. 13, showing linear growth in time for both (color figure online)

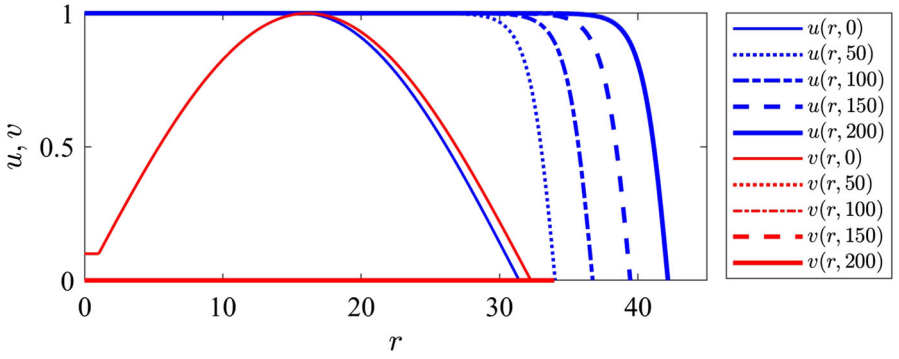

Fig. 15 Sample case (iii) in 2D with radial symmetry. Profiles of $u(r, t)$ (blue curve) and $v(r, t)$ (red curve) with $(\lambda_1, \lambda_2) = (10, 10.27)$ at time $t = 0, 50, 100, 150, 200$, showing the vanishing of v and the spreading of u like a traveling wave for large time (color figure online)

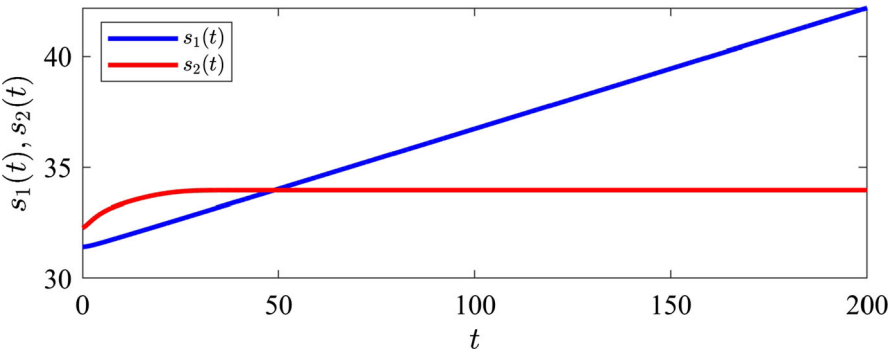

Fig. 16 Corresponding behaviour of $s_1(t)$ (blue curve) and $s_2(t)$ (red curve) in Fig. 15, showing $s_2(t)$ converging to a finite value and $s_1(t)$ growing linearly in time (color figure online)

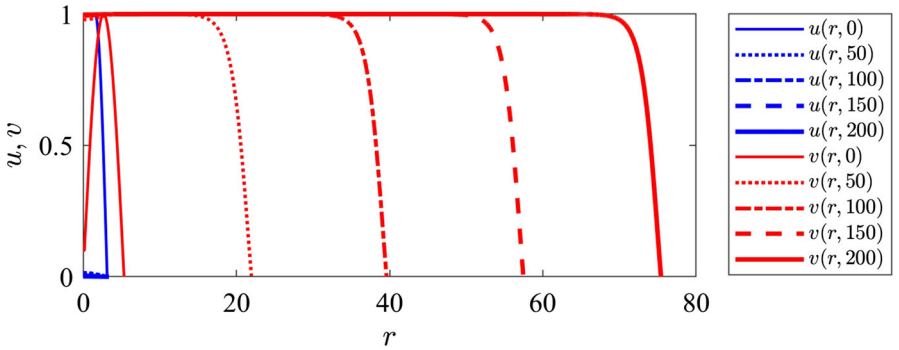

Fig. 17 Sample case (ii) in 2D with radial symmetry. Profiles of $u(r,t)$ (blue curve) and $v(r,t)$ (red curve) with $(\lambda_1, \lambda_2) = (1, 1.7)$ at time $t = 0, 50, 100, 150, 200$, showing the vanishing of u and the spreading of v like a traveling wave for large time (color figure online)

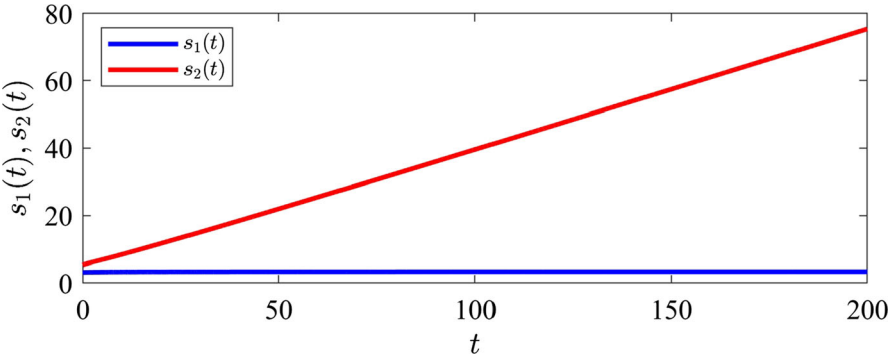

Fig. 18 Corresponding behaviour of $s_1(t)$ (blue curve) and $s_2(t)$ (red curve) in Fig. 17, showing $s_1(t)$ converging to a finite value and $s_2(t)$ growing linearly in time (color figure online)

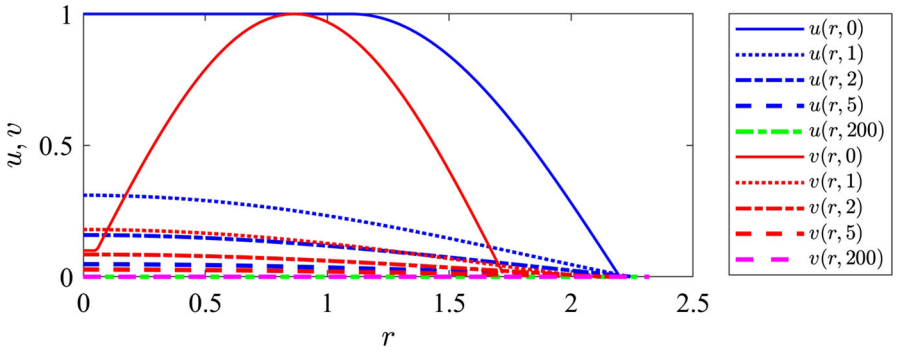

Fig. 19 Sample case (iv) in 2D with radial symmetry. Profiles of $u(r, t)$ (blue curve) and $v(r, t)$ (red curve) with $(\lambda_1, \lambda_2) = (0.70, 0.55)$ at time $t = 0, 1, 2, 5, 200$, showing the vanishing of both u and v for large time (color figure online)

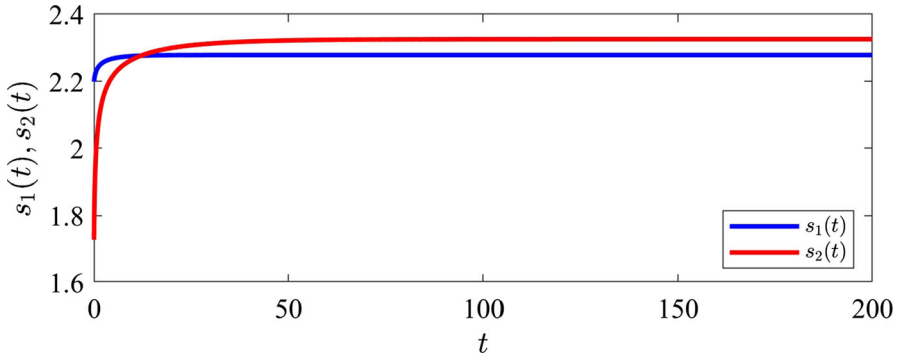

Fig. 20 Corresponding behaviour of $s_1(t)$ (blue curve) and $s_2(t)$ (red curve) in Fig. 19, showing both $s_1(t)$ and $s_2(t)$ converging to a finite value (color figure online)

and in case (iii), $\lim_{t\to\infty}[s_1(t) - s^*_{\mu_1} t] = \tilde{C}_1$ should be replaced by

$$\lim_{t\to\infty} \left\{ s_1(t) - \left[s^*_{\mu_1} t - c^*_1 \ln t \right] \right\} = \tilde{C}_1 \text{ for some } \tilde{C}_1 \in \mathbb{R}, \tag{2.7}$$

where $c^*_1 > 0$ and $c^*_2 > 0$ are positive constants independent of the initial data; see Du et al. (2015b).

These differences between the 1D and 2D cases are known as the "logarithmic shift" of the spreading for single species models. For two species models, like the one being considered in this paper, when both species spread successfully, whether there are similar logarithmic shifts for the spreading fronts is unknown so far. Note that for cases (ii) and (iii) here, it can be shown that the results of single species models can be applied, since for large time, the vanishing species can be neglected when examining the spreading profile of the winning species, that is the reason for the validity of (2.6) and (2.7).

Take the model parameters $(D, h, k, \gamma, \mu_1, \mu_2) = (2, 2, 0.5, 2, 0.1, 1)$, and $\lambda_1 = 10$, $\lambda_2 = 10.28$. Our simulations show that with these choices of parameters, for

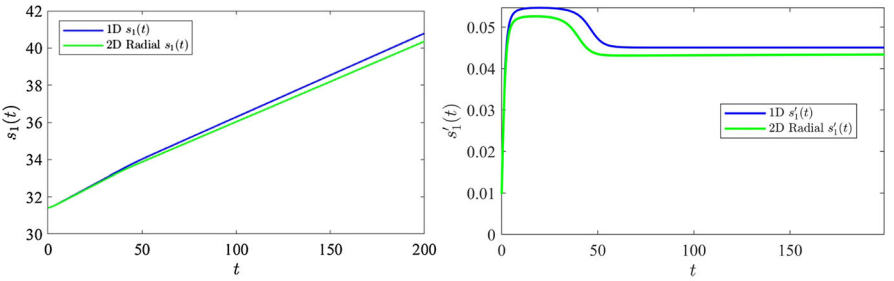

(A) $s_1(t)$ in 1D (blue curve) and 2D radial (green curve)

(B) $s_1'(t)$ in 1D (blue curve) and 2D radial (green curve)

Fig. 21 Comparison of $s_1(t)$ and $s_1'(t)$ in 1D and in 2D with radial symmetry

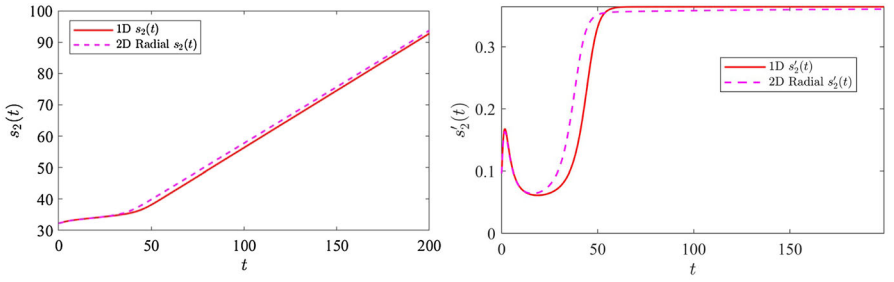

(A) $s_2(t)$ in 1D (solid curve) and 2D radial (dotted curve)

(B) $s_2'(t)$ in 1D (solid curve) and 2D radial (dotted curve)

Fig. 22 Comparison of $s_2(t)$ and $s_2'(t)$ in 1D and in 2D with radial symmetry

both the 1D case and the 2D radially symmetric case, the chase-and-run coexistence dynamics (namely case (i)) happens. While (1.11) holds regardless of the space dimension, no further theoretical results are available regarding possible logarithmic shifts of the free boundaries as in cases (ii) and (iii) mentioned above. In Figs. 21, 22, the fronts of both species in 1D, and in 2D with radial symmetry are shown. In particular, at $t = 200$, the front $s_1(t) \approx 40.7909$ with spreading speed $s_1'(t) \approx 0.045094$ in the 1D case, and $s_1(t) \approx 40.3574$ with spreading speed $s_1'(t) \approx 0.043409$ in the 2D radial case. On the other hand, for the front function $s_2(t)$, our simulations give $s_2(200) \approx 92.7642$ and $s_2'(200) \approx 0.364366$ in the 1D case, and $s_2(200) \approx 93.7160$ with $s_2'(200) \approx 0.360647$ in the 2D radial case. While these simulation results match those predicted by the theoretical result indicated in (1.11), we are not able to form any conclusion about the logarithmic shift based on them.

2.4 2D with triangular initial ranges

In two space dimensions without radial symmetry, the model should be formulated in the following form:

$$\begin{cases} u_t = D(u_{xx} + u_{yy}) + \gamma u(1 - u - kv) & \text{for } (x, y) \in \Omega_1(t),\ t > 0, \\ v_t = v_{xx} + v_{yy} + v(1 - v - hu) & \text{for } (x, y) \in \Omega_2(t),\ t > 0, \end{cases} \tag{2.8}$$

with the evolution of the free boundaries $\Gamma_i(t) := \partial\Omega_i(t)$, $i = 1, 2$, determined by

$$\begin{cases} u(x, y, t) = 0,\ (x, y) \in \Gamma_1(t), & t > 0, \\ v(x, y, t) = 0,\ (x, y) \in \Gamma_2(t), & t > 0, \end{cases} \tag{2.9}$$

and

$$\begin{cases} \mathbf{w_1}(x, y, t) = -\mu_1 \nabla u(x, y, t),\ t > 0,\ (x, y) \in \Gamma_1(t), \\ \mathbf{w_2}(x, y, t) = -\mu_2 \nabla v(x, y, t),\ t > 0,\ (x, y) \in \Gamma_2(t), \end{cases} \tag{2.10}$$

where $\mathbf{w_i}(x, y, t)$ is the velocity vector of the boundary point $(x, y) \in \Gamma_i(t)$, $i = 1, 2$; and

$$\nabla u(x, y, t) := (u_x(x, y, t), u_y(x, y, t)),\quad \nabla v(x, y, t) := (v_x(x, y, t), v_y(x, y, t)).$$

The initial conditions are

$$\begin{cases} u(x, y, 0) = u_0(x, y), & (x, y) \in \Omega_1(0), \\ v(x, y, 0) = v_0(x, y), & (x, y) \in \Omega_2(0). \end{cases} \tag{2.11}$$

We would like to point out that the above formulation of the problem is a natural extension of the one species model in Du and Guo (2012), Du et al. (2014), but for the competition system with free boundaries here, there is no theoretical result available so far in this general setting. Our numerical analysis here is the first treatment of the model with such generality.

In this subsection, we consider the case that the initial population ranges $\Omega_1(0)$ and $\Omega_2(0)$ are triangles centred at the origin $(0, 0)$, with $\Omega_i(0)$ the region enclosed by the straight lines

$$y = -\lambda_i\sqrt{3},\ y = \sqrt{3}\,x + 2\lambda_i\sqrt{3},\ y = -\sqrt{3}\,x + 2\lambda_i\sqrt{3},\quad i = 1, 2.$$

The initial populations $u_0(x, y, \lambda_1)$ and $v_0(x, y, \lambda_2)$ are given by

$$u_0(x, y, \lambda_1) = \phi_0(x, y, \lambda_1),\ v_0(x, y, \lambda_2) = \phi_0(x, y, \lambda_2),$$

with

$$\phi_0(x, y, \lambda_i) = \left(\frac{y}{\lambda_i} + \sqrt{3}\right)\left[\left(\sqrt{3} - \frac{y}{2\lambda_i}\right)^2 - \frac{3x^2}{4\lambda_i^2}\right],\ (x, y) \in \Omega_i(0),\ i = 1, 2.$$

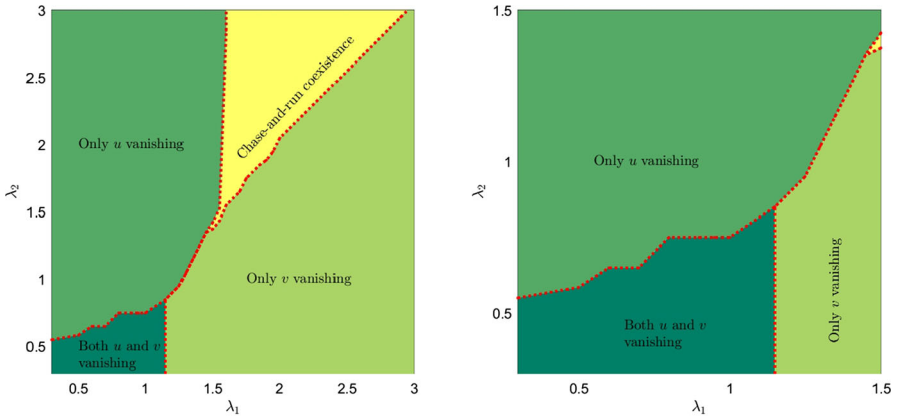

(A) $(\lambda_1, \lambda_2) \in [0.3, 3.0]^2$ **(B)** $(\lambda_1, \lambda_2) \in [0.3, 1.5]^2$

Fig. 23 Change of longtime dynamical behavior in 2D with triangular initial ranges as (λ_1, λ_2) varies

For this case, the level set method developed in Liu and Liu (2018) is applied to numerically simulate the model with $(D, h, k, \gamma, \mu_1, \mu_2) = (2, 2, 0.5, 2, 0.1, 1)$, time step $\Delta t = 3.125 \times 10^{-3}$, space mesh size $\Delta x = \Delta y = 0.25$ and simulations are run till $t = 120$. As in the previous subsections, to check the statements in Observation 1, we run type A and type B tests by varying λ_1 and λ_2 in the initial functions, chosen from a suitable range. Our simulation results again confirm the findings in Observation 1. The details of the chosen values of λ_1 and λ_2 are contained in Tables 5 and 6 in the Appendix of Khan et al. (2020).

In what follows, similar figures to that in the previous subsection are used to illustrate our numerical results.

These figures clearly exhibit the chase-and-run coexistence phenomenon (case (i)), as in the 1D and 2D radial cases examined in the previous subsections. Figures 24, 25, 26, 27 further show that both the free boundary and the population profile become nearly radially symmetric as time increases.

In the figures below, a sample of case (iii) is shown with $(\lambda_1, \lambda_2) = (2.0, 1.9)$, and a sample of case (ii) is shown for $(\lambda_1, \lambda_2) = (0.9, 1.0)$, while for $(\lambda_1, \lambda_2) = (0.7, 0.5)$, we obtain a sample of case (iv).

Remark In order to exhibit the free boundary behavior more clearly without costing too much CPU time, in the simulations to produce the samples for cases (i)-(iv) here, we have used $(\mu_1, \mu_2) = (0.6, 2)$ instead of $(0.1, 1)$; this change causes the free boundaries to move faster and therefore reveals the longtime behavior more clearly.

3 Time-Periodic environment

In this section, we use numerical calculation to check whether the chase-and-run dynamics (case (i)) persists under time-periodic perturbations of the environment, and

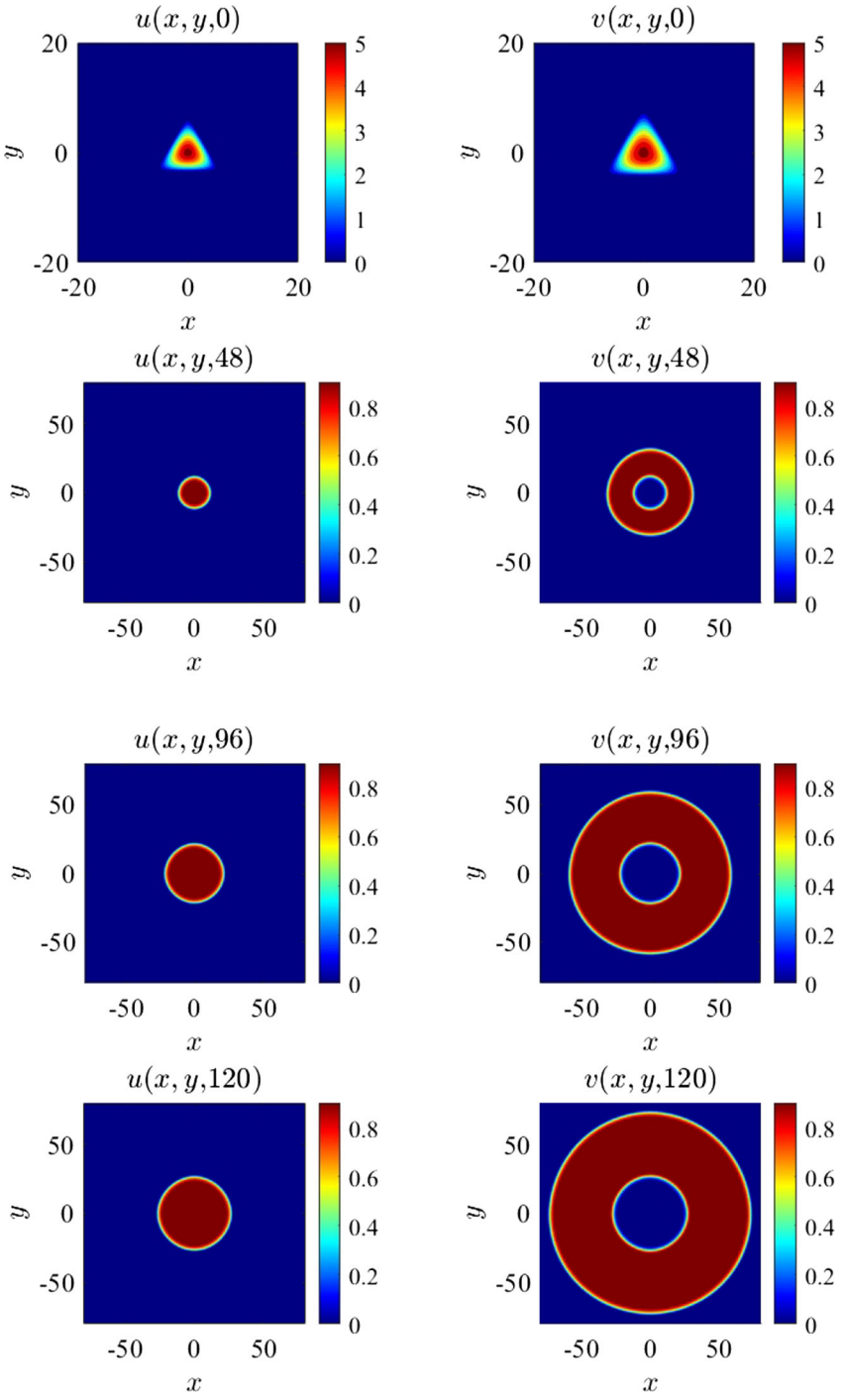

Fig. 24 Sample of case (i) in 2D with triangular initial ranges. Profiles of u and v with $(\lambda_1, \lambda_2) = (2.0, 2.5)$ at $t = 0, 48, 96, 120$

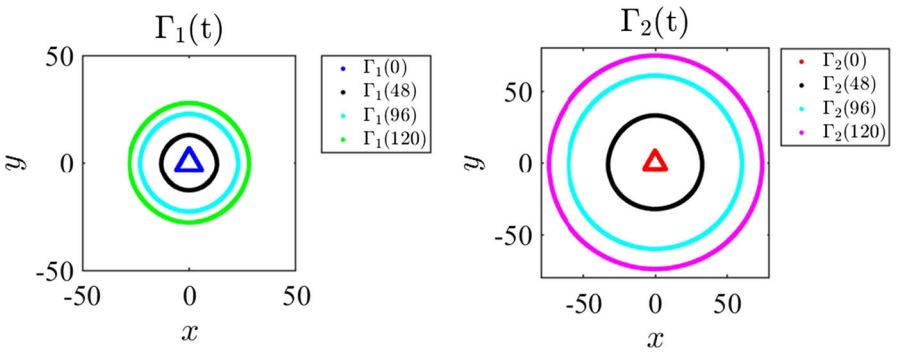

Fig. 25 Corresponding snapshots of the moving boundaries $\Gamma_1(t)$ and $\Gamma_2(t)$ in Fig. 24

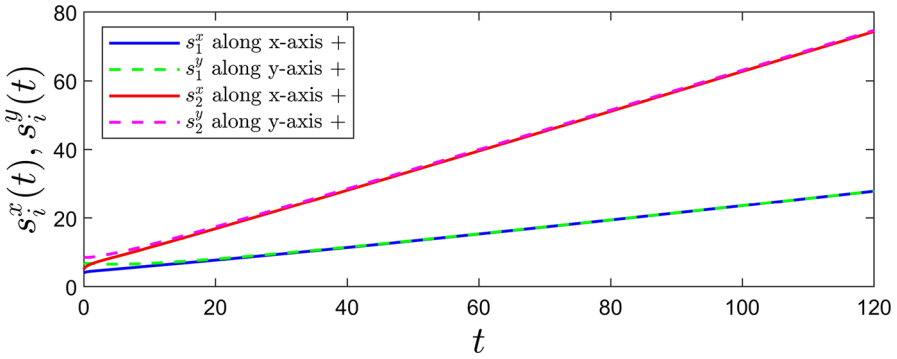

Fig. 26 The curves $s_i^x(t) := \Gamma_i(t) \cap \{y = 0\}$, $s_i^y(t) := \Gamma_i(t) \cap \{x = 0\}$, $i = 1, 2$ of the corresponding moving boundaries in Fig. 25 exhibit linear growth in time

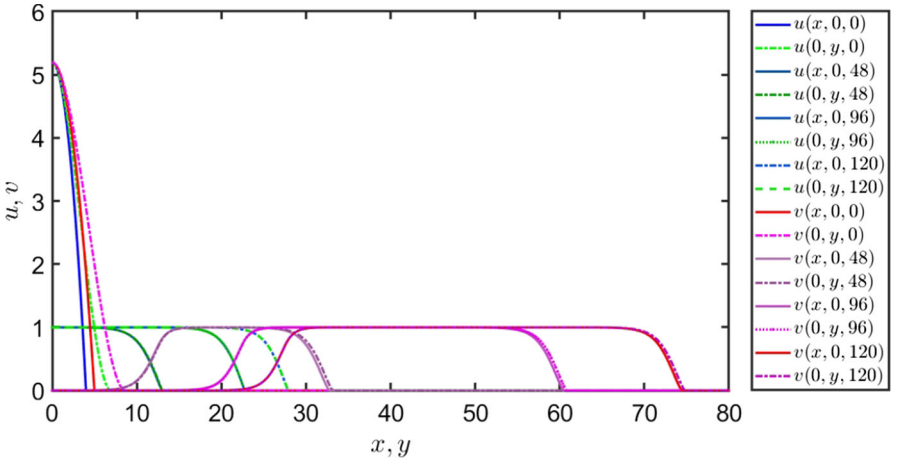

Fig. 27 Profile of $u(x, 0, t)$, $u(0, y, t)$, $v(x, 0, t)$, $v(0, y, t)$ at $t = 0, 48, 96, 120$ obtained from the population distribution in Fig. 24. They propagate like traveling waves in both the x and y directions

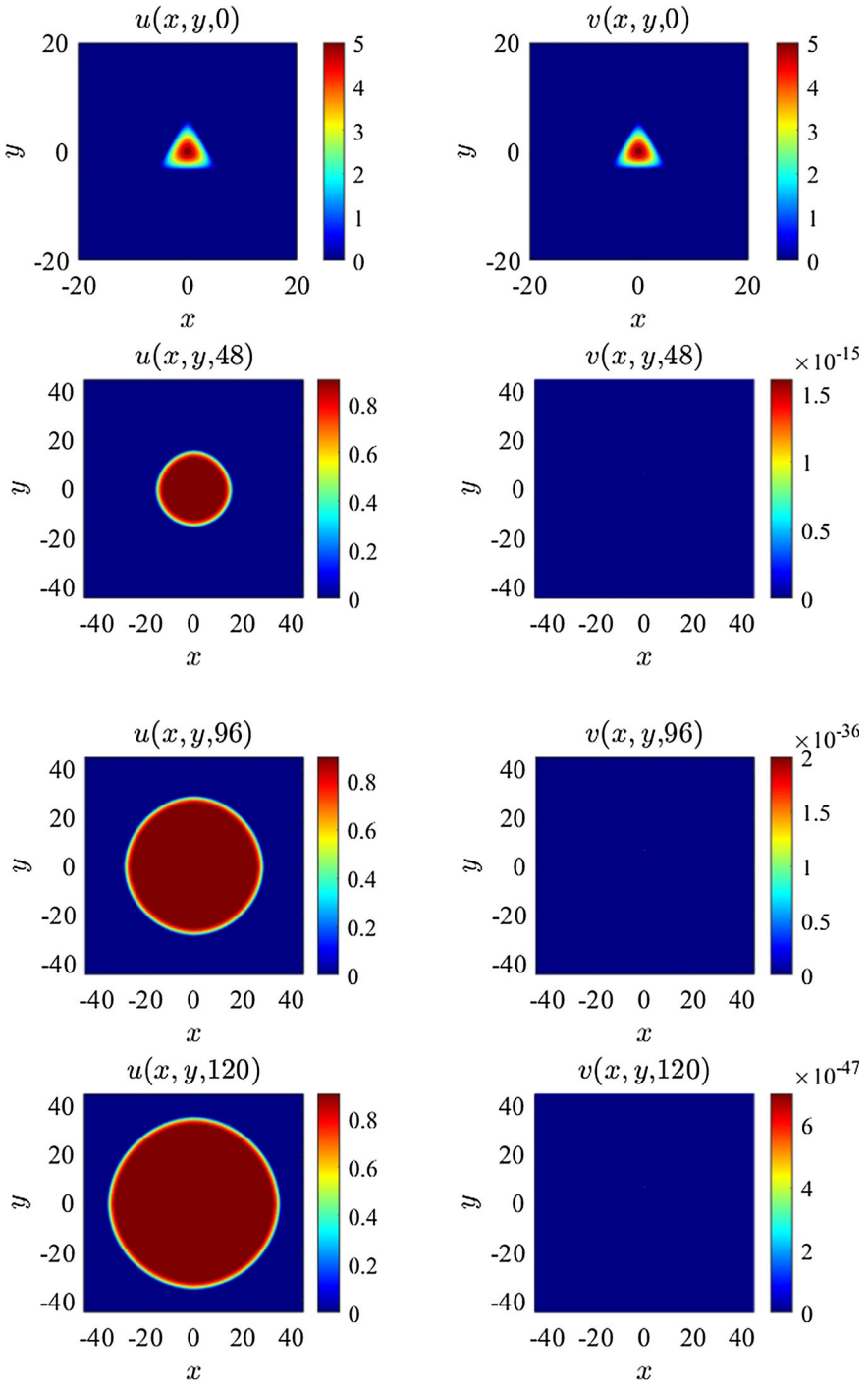

Fig. 28 Sample of case (iii) in 2D with triangular initial ranges. Profiles of u and v with $(\lambda_1, \lambda_2) = (2.0, 1.9)$ at $t = 0, 48, 96, 120$, with that of u becoming circular as time increases

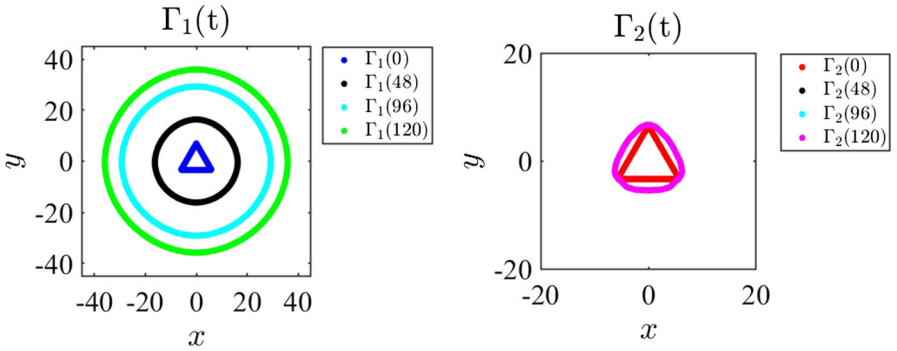

Fig. 29 Corresponding snapshots of the moving boundaries $\Gamma_1(t)$ and $\Gamma_2(t)$ in Fig. 28. Note that the movement of $\Gamma_2(t)$ after $t = 48$ is so small that it cannot be observed here

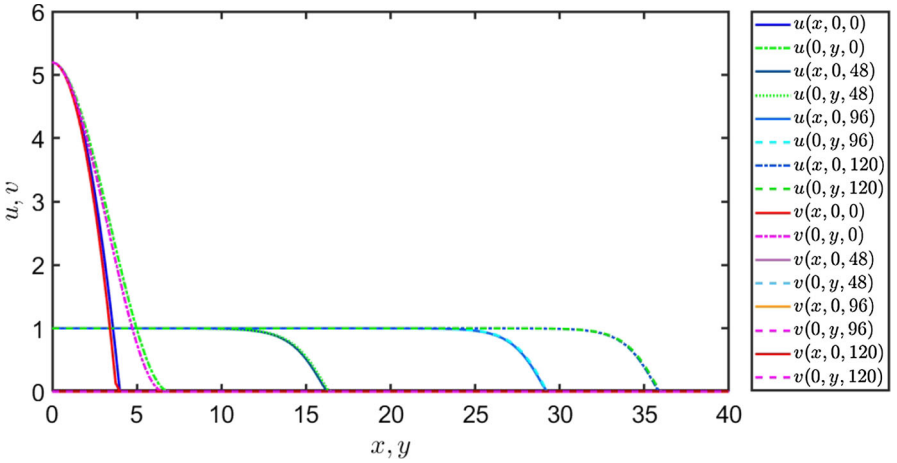

Fig. 30 Profiles of $u(x, 0, t)$, $u(0, y, t)$, $v(x, 0, t)$, $v(0, y, t)$ at $t = 0, 48, 96, 120$ obtained from the corresponding population distribution in Fig. 28, where u propagates like a traveling wave in both the x and y directions

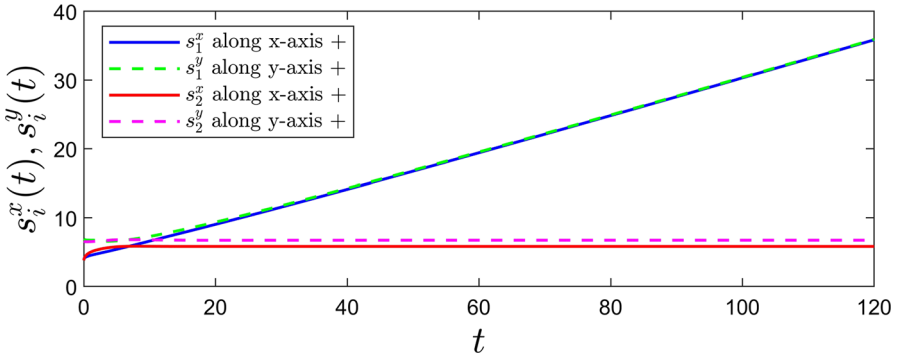

Fig. 31 The curves $s_i^x(t) := \Gamma_i(t) \cap \{y = 0\}$, $s_i^y(t) := \Gamma_i(t) \cap \{x = 0\}$ $(i = 1, 2)$ obtained from the moving boundaries in Fig. 29, where $s_1^x(t)$ and $s_1^y(t)$ grow linearly, while $s_2^x(t)$ and $s_2^y(t)$ approach a constant as t increases

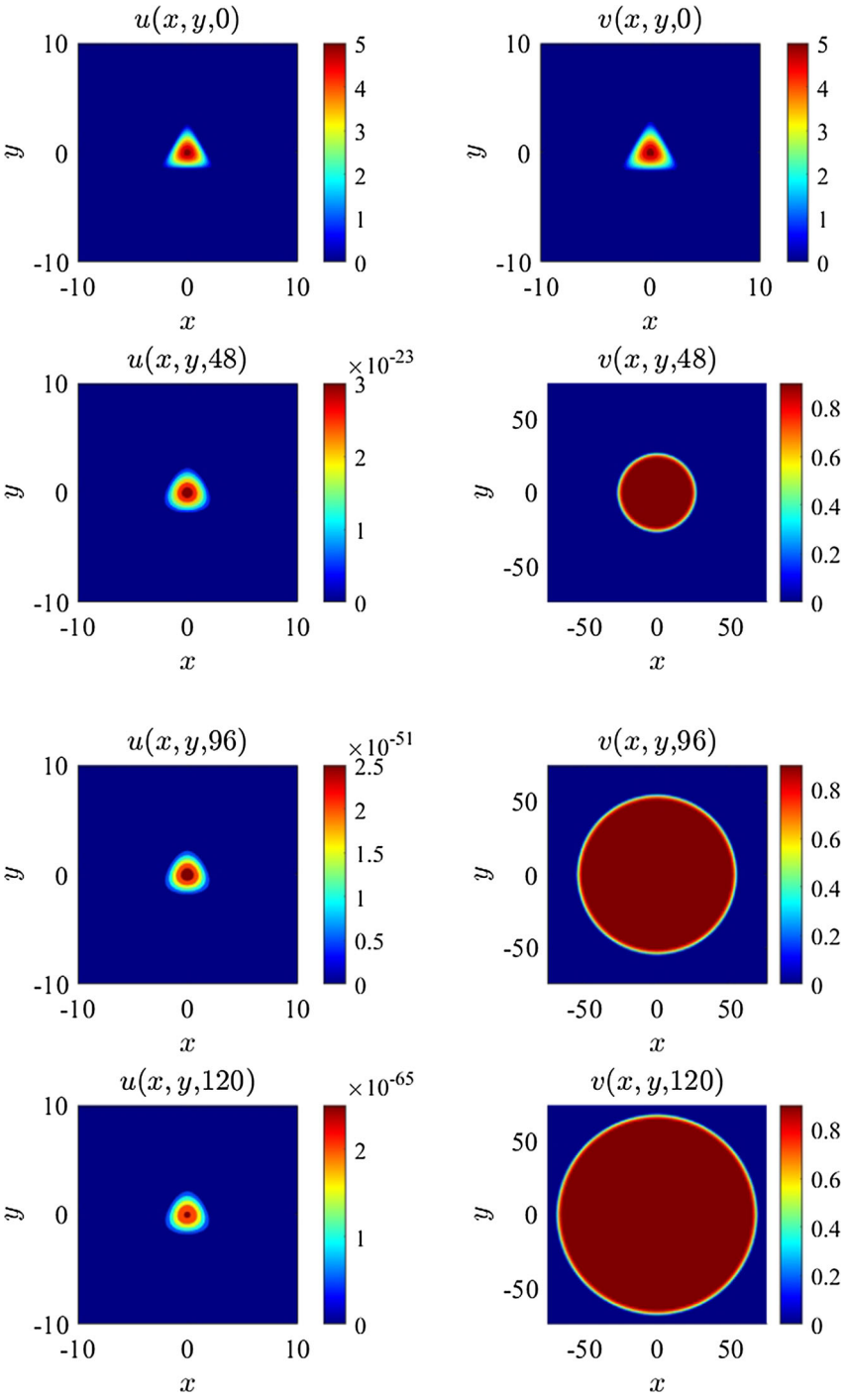

Fig. 32 Sample case (ii) in 2D with triangular initial ranges. Profiles of u and v with $(\lambda_1, \lambda_2) = (0.9, 1.0)$ at $t = 0, 48, 96, 120$, with that of v becoming circular as time increases

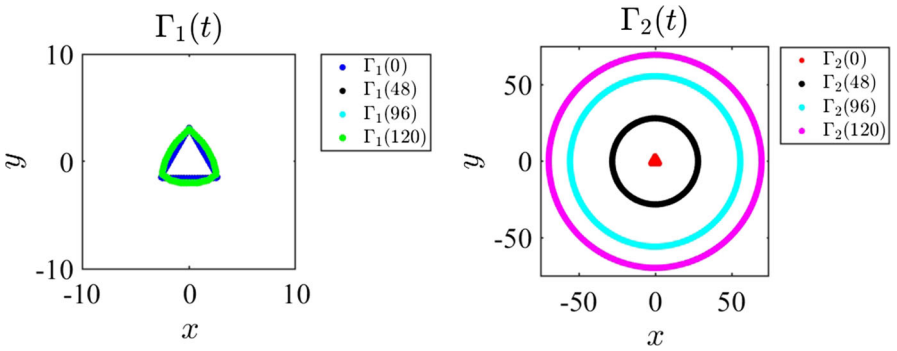

Fig. 33 Snapshots of corresponding moving boundaries $\Gamma_1(t)$ and $\Gamma_2(t)$ in Fig. 32

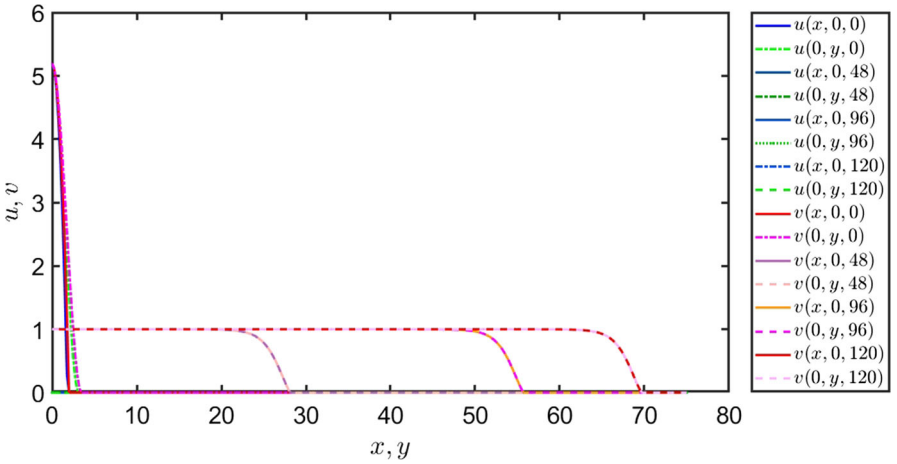

Fig. 34 Profiles of $u(x,0,t)$, $u(0,y,t)$, $v(x,0,t)$, $v(0,y,t)$ at $t = 0, 48, 96, 120$ obtained from the population distribution in Fig. 32, where v propagates like a traveling wave in both the x and y directions

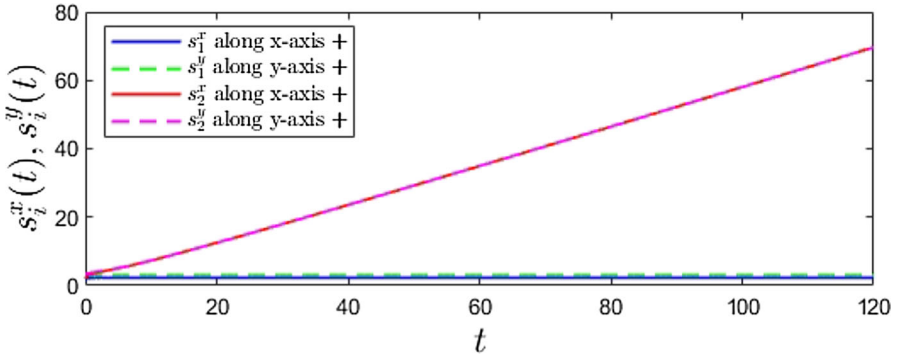

Fig. 35 Curves $s_i^x(t) := \Gamma_i(t) \cap \{y = 0\}$, $s_i^y(t) := \Gamma_i(t) \cap \{x = 0\}$ $(i = 1, 2)$ obtained from the moving boundaries in Fig. 33, where $s_2^x(t)$ and $s_2^y(t)$ grow linearly, while $s_1^x(t)$ and $s_1^y(t)$ approach a constant as t increases

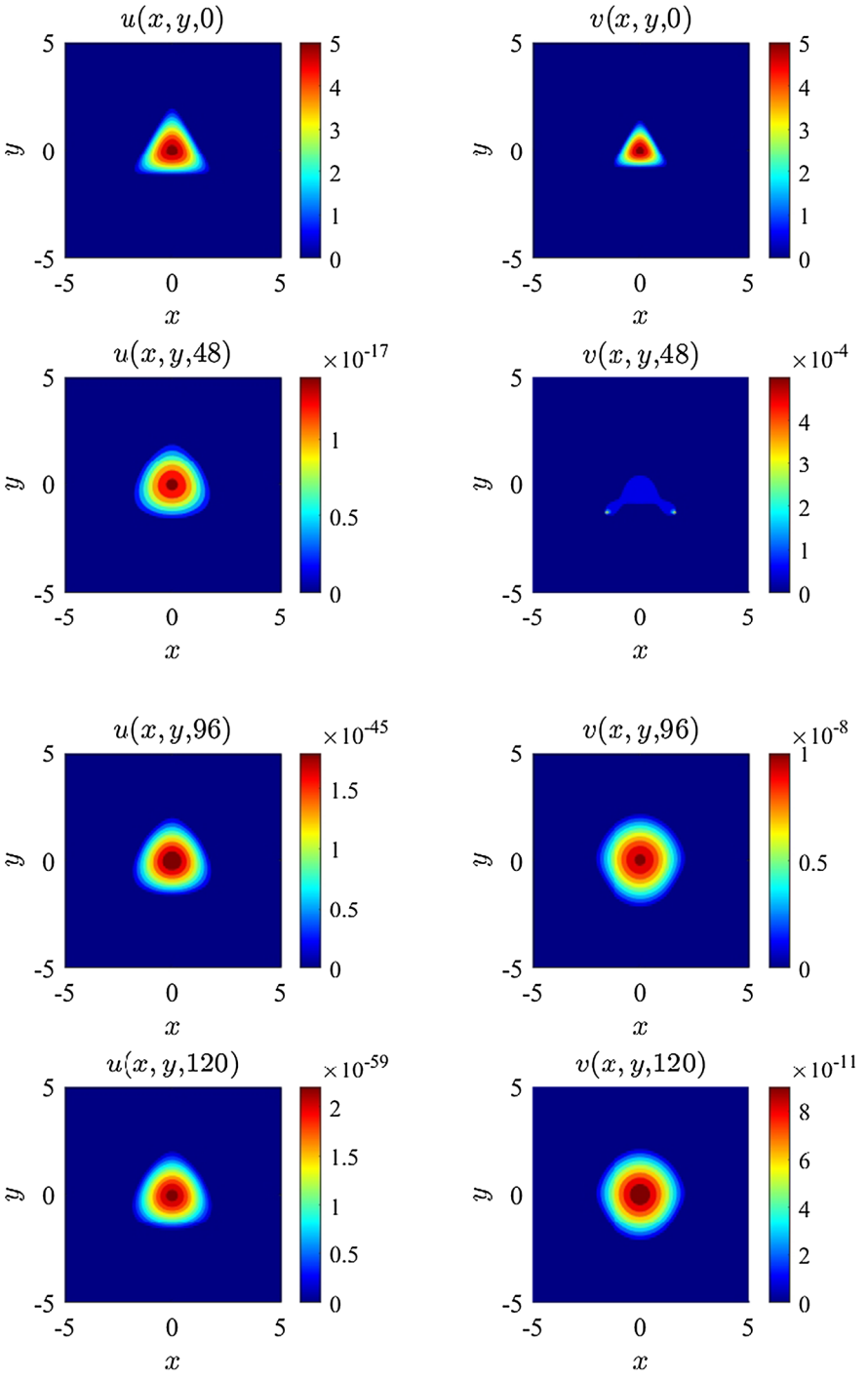

Fig. 36 Sample of case (iv) in 2D with triangular initial ranges. Profiles of u and v with $(\lambda_1, \lambda_2) = (0.7, 0.5)$ at $t = 0, 48, 96, 120$

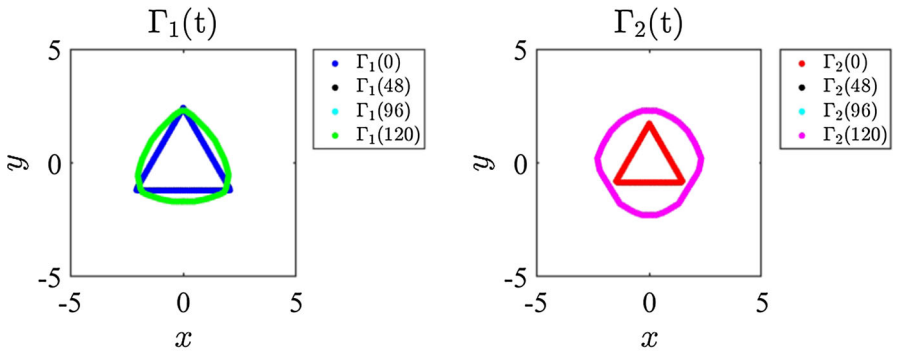

Fig. 37 Snapshots of corresponding moving boundaries $\Gamma_1(t)$ and $\Gamma_2(t)$ in Fig. 36. (The movements of the boundaries are so small that they cannot be observed here after $t = 48$)

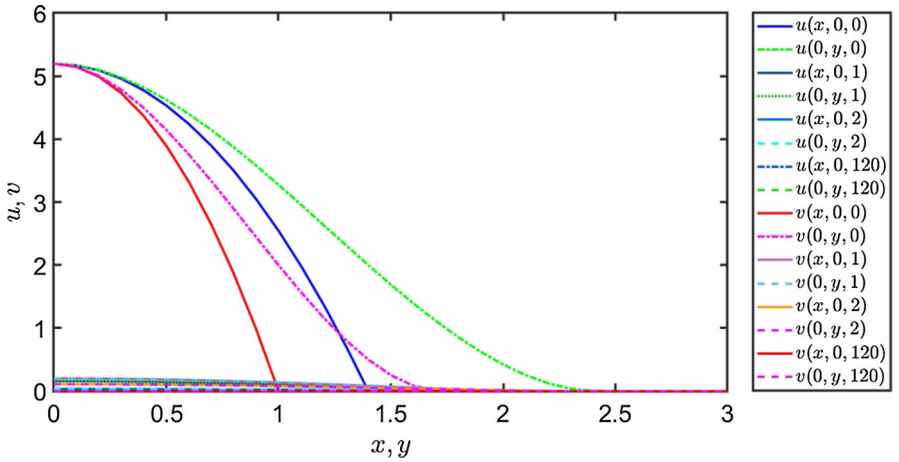

Fig. 38 Profiles of $u(x, 0, t)$, $u(0, y, t)$, $v(x, 0, t)$, $v((0, y, t)$ at $t = 0, 48, 96, 120$, obtained from the population distribution in Fig. 36

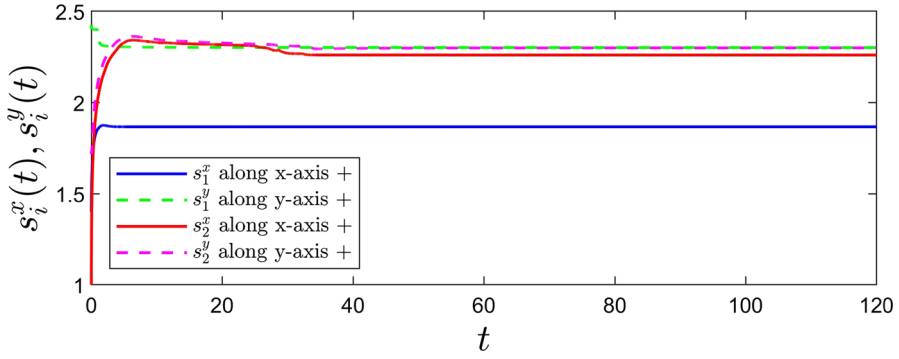

Fig. 39 The curves $s_i^x(t) := \Gamma_i(t) \cap \{y = 0\}$, $s_i^y(t) := \Gamma_i(t) \cap \{x = 0\}$ $(i = 1, 2)$ obtained from the moving boundaries in Fig. 37, converging to constants as t increases

if so, how the spreading speeds of the species are affected. We have the following observations from the numerical experiments here.

Observation 2 *The chase-and-run dynamics demonstrated in Sect. 2 are retained under time-periodic perturbation of the environment, and the spreading speeds of the species are not altered much by this perturbation.*

3.1 Time-periodic perturbation in 1D

For each of the situations examined in Sect. 2 for the 1D case, we replace the growth functions in the model by

$\gamma u(1+\epsilon_1(t)-u-kv)$ in the u equation, and $v(1+\epsilon_2(t)-v-hu)$ in the v equation,

where

$$\epsilon_i(t)=\sigma_i \sin\left(\frac{2\pi t}{T}\right),\ i=1,2,$$

with T, σ_1, σ_2 positive constants. Clearly $\epsilon_i(t)$ are periodic functions of time t with period T. Moreover,

$$\int_0^T \epsilon_i(t)dt=0,\quad i=1,2.$$

In other words, the intrinsic growth rates of u and v in the model are changed from γ and 1 to $\gamma+\gamma\epsilon_1(t)$ and $1+\epsilon_2(t)$, respectively, to reflect the assumption that the homogeneous environment is now changed to a time-periodic environment with period T, but with the average effect to the species the same as in the homogeneous environment. The parameters σ_1 and σ_2 measure the magnitude of the oscillation of the environment felt by u and v, respectively.

Figure 40 shows several snapshots of $u(x,t)$ and $v(x,t)$ between times $t=120$ and 121, where the parameters values are taken as follows: $(D,h,k,\gamma,\mu_1,\mu_2)=(2,2,0.5,2,0.1,1)$, $T=1, \sigma_1=\sigma_2=1, \lambda_1=10, \lambda_2=10.5$, time step $\Delta t=5\times10^{-6}$, grid size $\Delta x=0.01$, and the initial functions (u_0,v_0) are the same as in (2.1) and (2.2).

Correspondingly,

$$s_1^0=\lambda_1\pi \text{ and } s_2^0=\lambda_2\pi.$$

Figure 41 shows the behaviour of the corresponding front functions $s_1(t)$ and $s_2(t)$.

These figures show that the species exhibit the chase-and-run dynamics, and the snapshots in Fig. 40 further indicate that, during the spreading process, u and v oscillate synchronously with the time-periodic environment. Figure 41 indicates that the spreading fronts advance linearly in time albeit with small periodic variations of period 1.

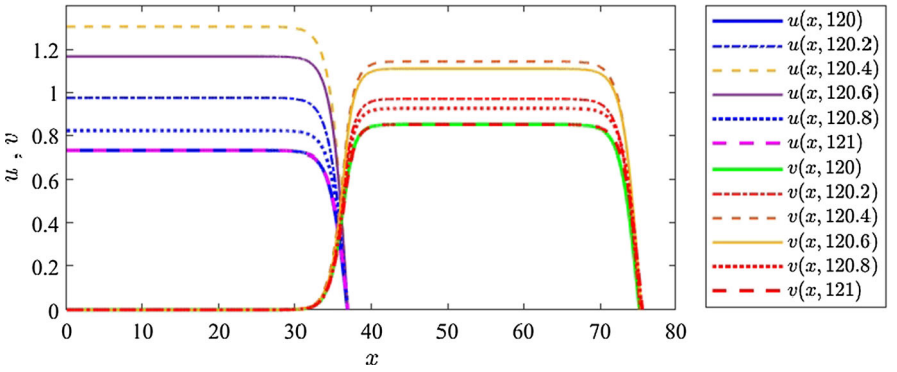

Fig. 40 Population distribution in 1D with time-periodic environment of period $T = 1$ and magnitude of the oscillations $\sigma_1 = \sigma_2 = 1$. Population curve of u at time $t = 120$ (solid blue curve) coincides with population curve of u at time $t = 121$ (magenta dotted curve), and population curve of v at time $t = 120$ (solid green curve) coincides with population curve of v at time $t = 121$ (red dotted curve), indicating time-periodic variation of the population induced by the time-periodic environment during the spreading process

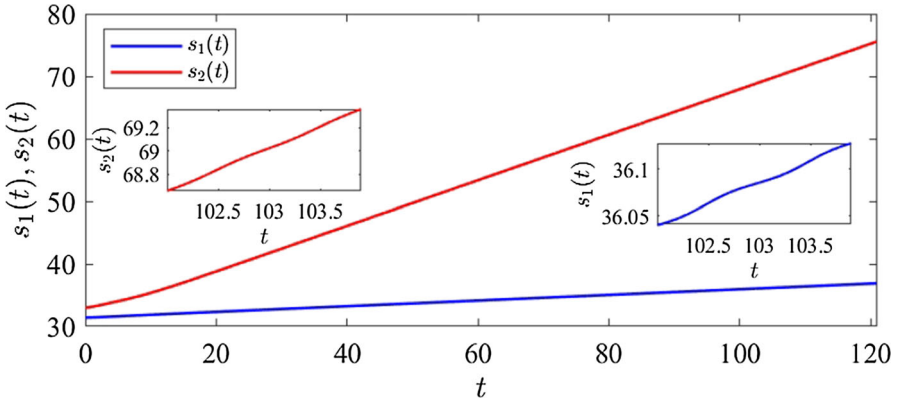

Fig. 41 Spreading fronts of the species in 1D time-periodic case with period $T = 1$, magnitude of the oscillations $\sigma_1 = \sigma_2 = 1$ up to time $t = 120$

To see how the time-periodic perturbation affects the spreading speed, we have checked the influence of the magnitude of the oscillations numerically for a series of values of $\sigma_1, \sigma_2 \in (0, 1]$. The simulation results are summarized in Tables 1, 2, 3, where each simulation is run until $t = 120$ with time step $\Delta t = 5 \times 10^{-6}$, space step $\Delta x = 0.01$, and all the other parameter values the same as in Figs. 40 and 41. For the time-periodic cases with $T = 1$, the average speed

$$\overline{s_i'(t)} := \int_t^{t+1} s_i'(s)ds, \quad i = 1, 2$$

is used. The simulation results suggest that these time-periodic perturbations do not change much of the spreading speeds of the two populations.

Table 1 $\sigma_1 = \sigma_2$

$\sigma_1 = \sigma_2$

σ_1	σ_2	**Homogeneous** $s_1'(120)$	**Time-Periodic** $\overline{s_1'(120)}$	**Homogeneous** $s_2'(120)$	**Time-Periodic** $\overline{s_2'(120)}$
0.01	0.01	0.045093	0.045093	0.364369	0.364363
0.05	0.05	0.045093	0.045094	0.364369	0.364363
0.1	0.1	0.045093	0.045095	0.364369	0.364361
0.5	0.5	0.045093	0.045127	0.364369	0.364311
1.0	1.0	0.045093	0.045224	0.364369	0.364154

Table 2 $\sigma_1 > \sigma_2$

$\sigma_1 > \sigma_2$

σ_1	σ_2	**Homogeneous** $s_1'(120)$	**Time-Periodic** $\overline{s_1'(120)}$	**Homogeneous** $s_2'(120)$	**Time-Periodic** $\overline{s_2'(120)}$
0.01	0.001	0.045093	0.045093	0.364369	0.364364
0.05	0.005	0.045093	0.045094	0.364369	0.364364
0.1	0.01	0.045093	0.045095	0.364369	0.364364
0.5	0.05	0.045093	0.045132	0.364369	0.364363
1	0.1	0.045093	0.045246	0.364369	0.364361

Table 3 $\sigma_1 < \sigma_2$

$\sigma_1 < \sigma_2$

σ_1	σ_2	**Homogeneous** $s_1'(120)$	**Time-Periodic** $\overline{s_1'(120)}$	**Homogeneous** $s_2'(120)$	**Time-Periodic** $\overline{s_2'(120)}$
0.001	0.01	0.045093	0.045093	0.364369	0.364364
0.005	0.05	0.045093	0.045093	0.364369	0.364363
0.01	0.1	0.045093	0.045093	0.364369	0.364361
0.05	0.5	0.045093	0.045093	0.364369	0.364311
0.1	1	0.045093	0.045093	0.364369	0.364154

Some samples of the speed functions $s_1'(t)$ and $s_2'(t)$ for the time-periodic case are shown in Figures 42, 43 and 44, where the magnitude of the environmental oscillation felt by the species is clearly reflected by the magnitude of the oscillation of the speed function of the corresponding species, though the average speed is not affected much, as already mentioned above.

3.2 Time-periodic perturbation in 2D

For the 2D radially symmetric case and the 2D case with triangular initial ranges, we have run parallel numerical simulations to that in the previous subsection, and similar findings are observed. The details are omitted.

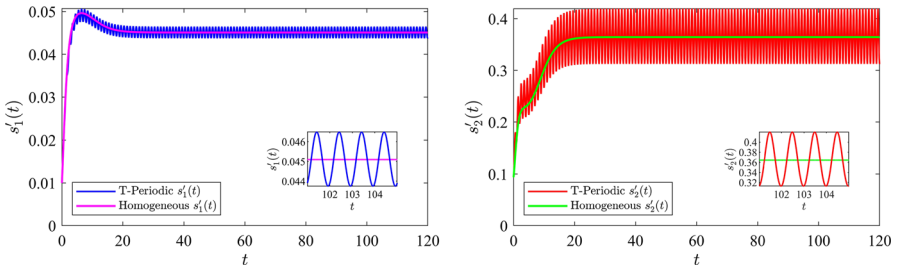

Fig. 42 Speed of the spreading front of the species u (left) and v (right) in homogeneous and time-periodic environment with period $T = 1$ and magnitude of the oscillations $\sigma_1 = 0.1, \sigma_2 = 1$

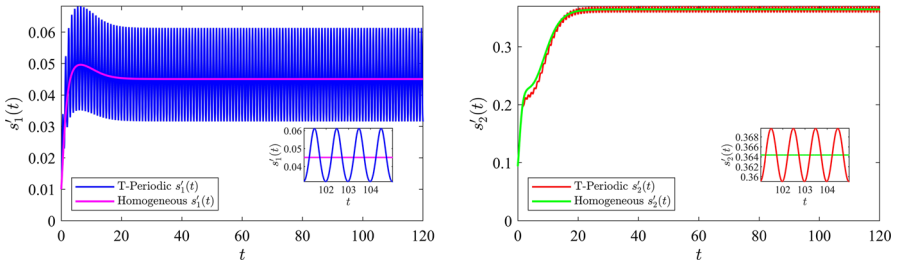

Fig. 43 Speed of the spreading front of the species u (left) and v (right) in homogeneous and time-periodic environment with period $T = 1$ and magnitude of the oscillations $\sigma_1 = 1, \sigma_2 = 0.1$

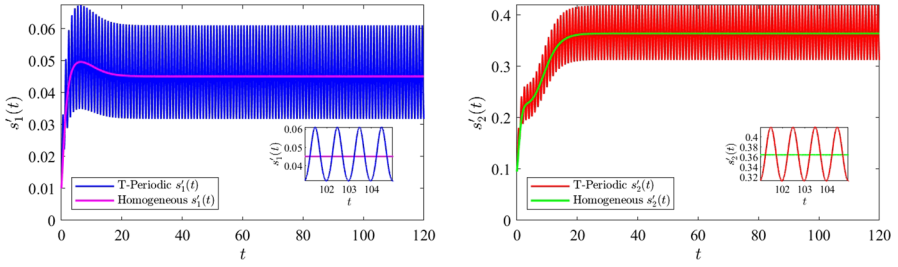

Fig. 44 Speed of the spreading front of the species u (left) and v (right) in homogeneous and time-periodic environment with period $T = 1$ and magnitude of the oscillations $\sigma_1 = 1, \sigma_2 = 1$

4 Asymptotic shape of the population ranges in 2D

Our simulation results in Sect. 2.4 with triangular initial population ranges reveal the following findings.

Observation 3 *If the species u (resp. v) invades successfully, then the shape of its invading fronts, namely $\Gamma_1(t)$ (resp. $\Gamma_2(t)$) becomes more and more circular as time increases.*

In the case of a single species model, this phenomenon has been rigorously established in Du et al. (2014). For models with two species, this is unknown so far.

To obtain further support to the findings in Observation 3, we now look at the case that the initial population ranges are rectangles in $\mathbb{R}^2$, and run parallel numerical

experiments to that in Sect. 2.4. More precisely, we take $\Omega_i(0)$ the rectangle enclosed by the straight lines $x = \pm\frac{3}{2}\lambda_i$, $y = \pm\lambda_i$ $(i = 1, 2)$, and the initial functions are given by

$$u_0(x, y, \lambda_1) = \psi_0(x, y, \lambda_1),\ v_0(x, y, \lambda_2) = \psi_0(x, y, \lambda_2),$$

with

$$\psi_0(x, y, \lambda_i) := \left(\frac{3}{2} - \frac{x}{\lambda_i}\right)\left(\frac{3}{2} + \frac{x}{\lambda_i}\right)\left(1 - \frac{y}{\lambda_i}\right)\left(1 + \frac{y}{\lambda_i}\right),\ (x, y) \in \Omega_i(0).$$

Figures 45, 46, 47, 48 display a sample case of chase-and-run dynamics, where the population ranges (as well as the spatial population distributions) are becoming more and more circular as time increases. This simulation is done with parameters $(D, h, k, \gamma, \mu_1, \mu_2) = (2, 2, 0.5, 2, 0.6, 2)$, time step $\Delta t = 3.125 \times 10^{-3}$, grid size $\Delta x = \Delta y = 0.25$, and initial data determined by taking $\lambda_1 = 2.2$ and $\lambda_2 = 2.3$. The simulation is run until $t = 120$.

Figures 49, 50, 51, 52 show a sample case that v vanishes and u invades successfully, and the population range of u as well as the spatial distribution of u become more and more circular as time increases. Note, however, that the population range of the vanishing species v does not become circular as time increases. Here the parameters are the same as in the Figures immediately above except that the initial data are obtained with $(\lambda_1, \lambda_2) = (2.1, 2.0)$.

Figures 53, 54, 55, 56 describe a sample case that u vanishes and v invades successfully, obtained by taking $(\lambda_1, \lambda_2) = (1.9, 2.0)$, with the other parameters unchanged.

It is now clear that these numerical results support the findings in Observation 3 in the same way as those in Sect. 2.4 where triangular initial ranges were used.

5 Further discussions

In this paper, we have tried to find all the possible scenarios when two invasive species are competing and invading the environment at the same time, based on a suitable mathematical model. More precisely, we have numerically examined the invasive behavior of two competing species via a Lotka-Volterra competition model with diffusion and free boundaries. The parameters in the reaction terms of the model are chosen in such a way that when spatial variation in the model is ignored, one species will survive the competition (and thus named the strong species) and the other will vanish (named the weak species). In 1D and in 2D with radial symmetry, some theoretical results on this diffusive model with free boundary already exist (see Du and Wu (2018)), but a full picture of the model is still lacking. Here through numerical experiments with parametrized initial functions, a classification of four types of longtime dynamical behavior emerges, namely (i) chase-and-run coexistence, (ii) vanishing of the strong species with the weak species invading successfully, (iii) vanishing of the weak species with the strong species invading successfully, (iv) vanishing of both species.

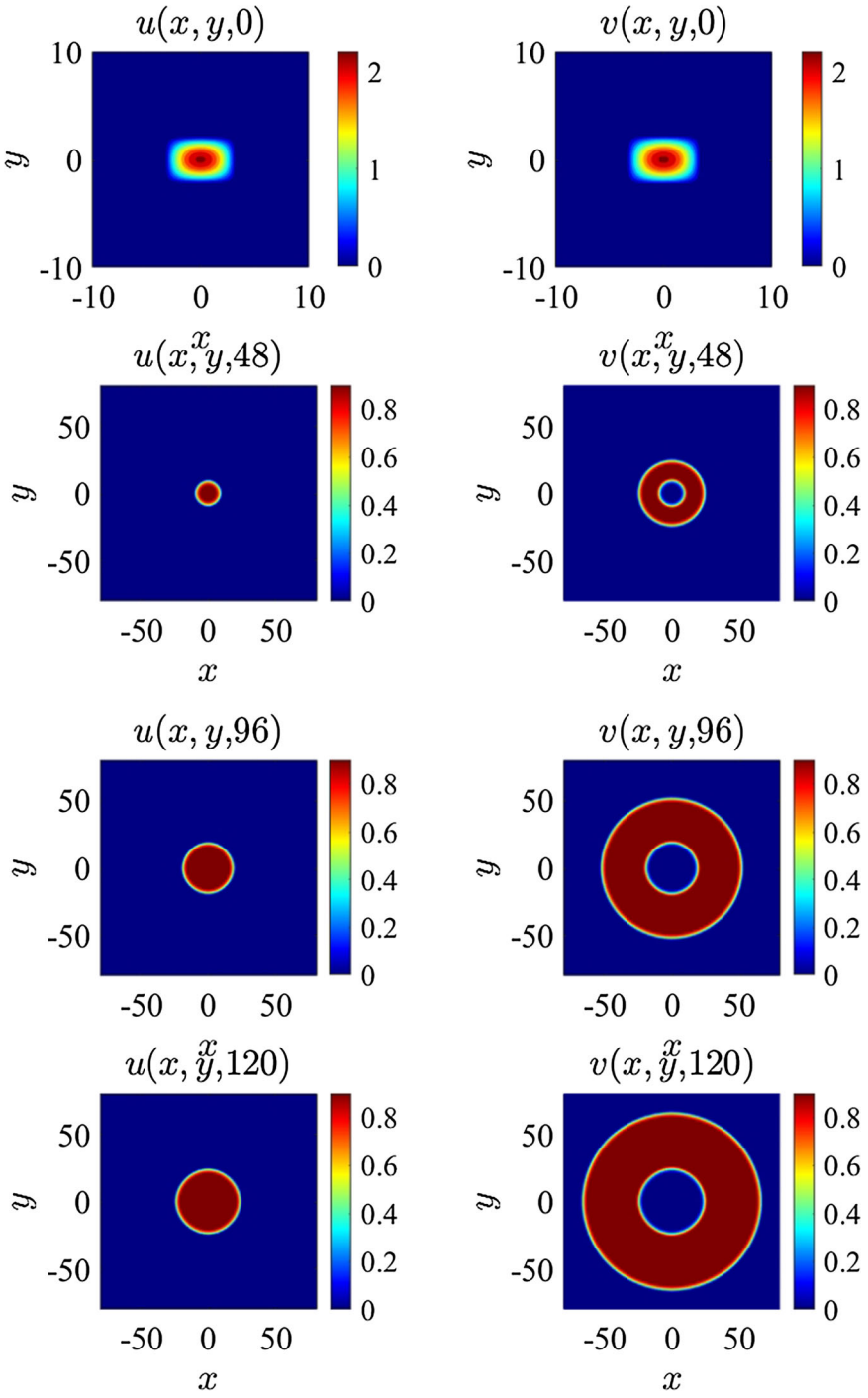

Fig. 45 Profiles of u and v with $(\lambda_1, \lambda_2) = (2.2, 2.3)$ at $t = 0, 48, 96, 120$, showing chase-and-run dynamics, with the profiles of u and v becoming circular as time increases

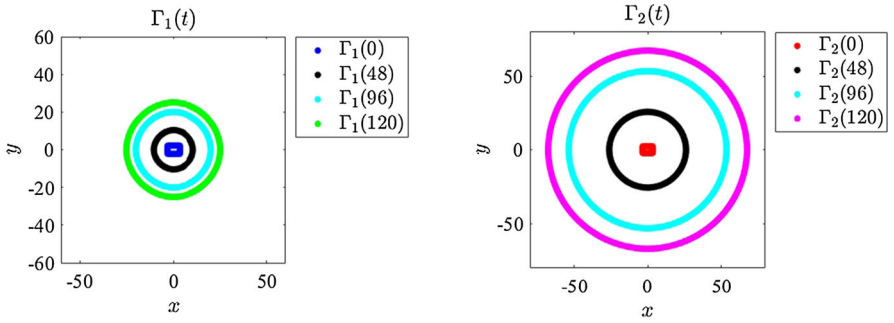

Fig. 46 Corresponding behaviour of $\Gamma_1(t)$ and $\Gamma_2(t)$ in Fig. 45 at time $t = 0, 48, 96, 120$; their shapes become circular as time increases

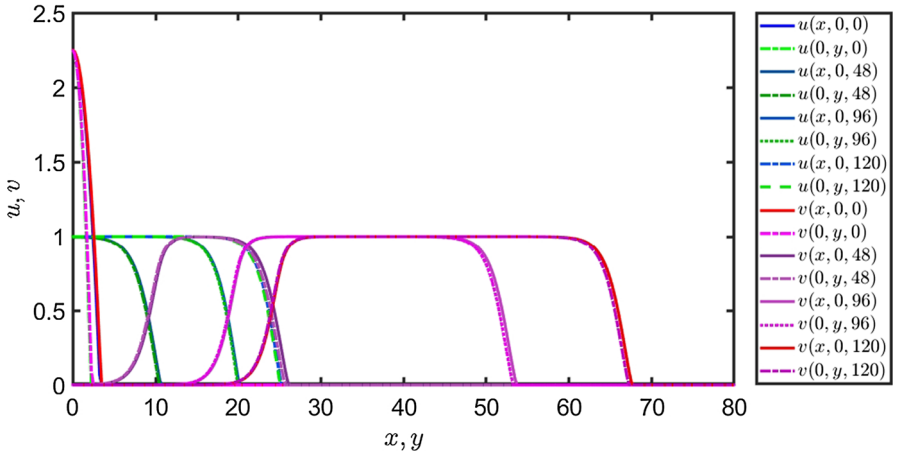

Fig. 47 Profiles of $u(x, 0, t)$, $u(0, y, t)$, $v(x, 0, t)$, $v(0, y, t)$ at $t = 0, 48, 96, 120$, obtained from the population distribution in Fig. 45. They propagate like traveling waves in both the x and y directions

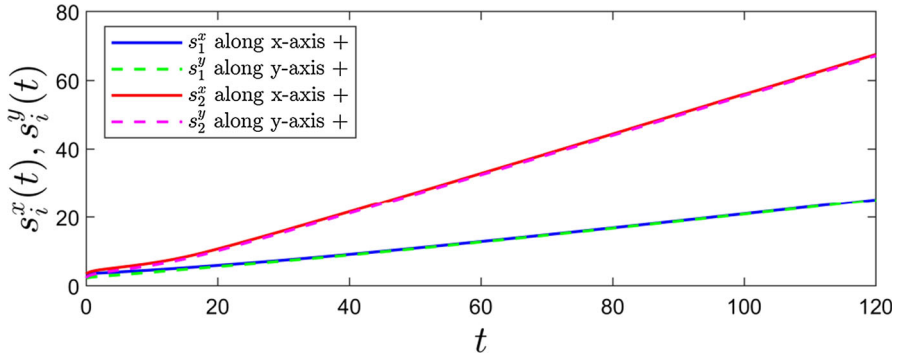

Fig. 48 The curves $s_i^x(t) := \Gamma_i(t) \cap \{y = 0\}$, $s_i^y(t) := \Gamma_i(t) \cap \{x = 0\}$ $(i = 1, 2)$ obtained from the corresponding moving boundaries in Fig. 46, showing linear growth in time

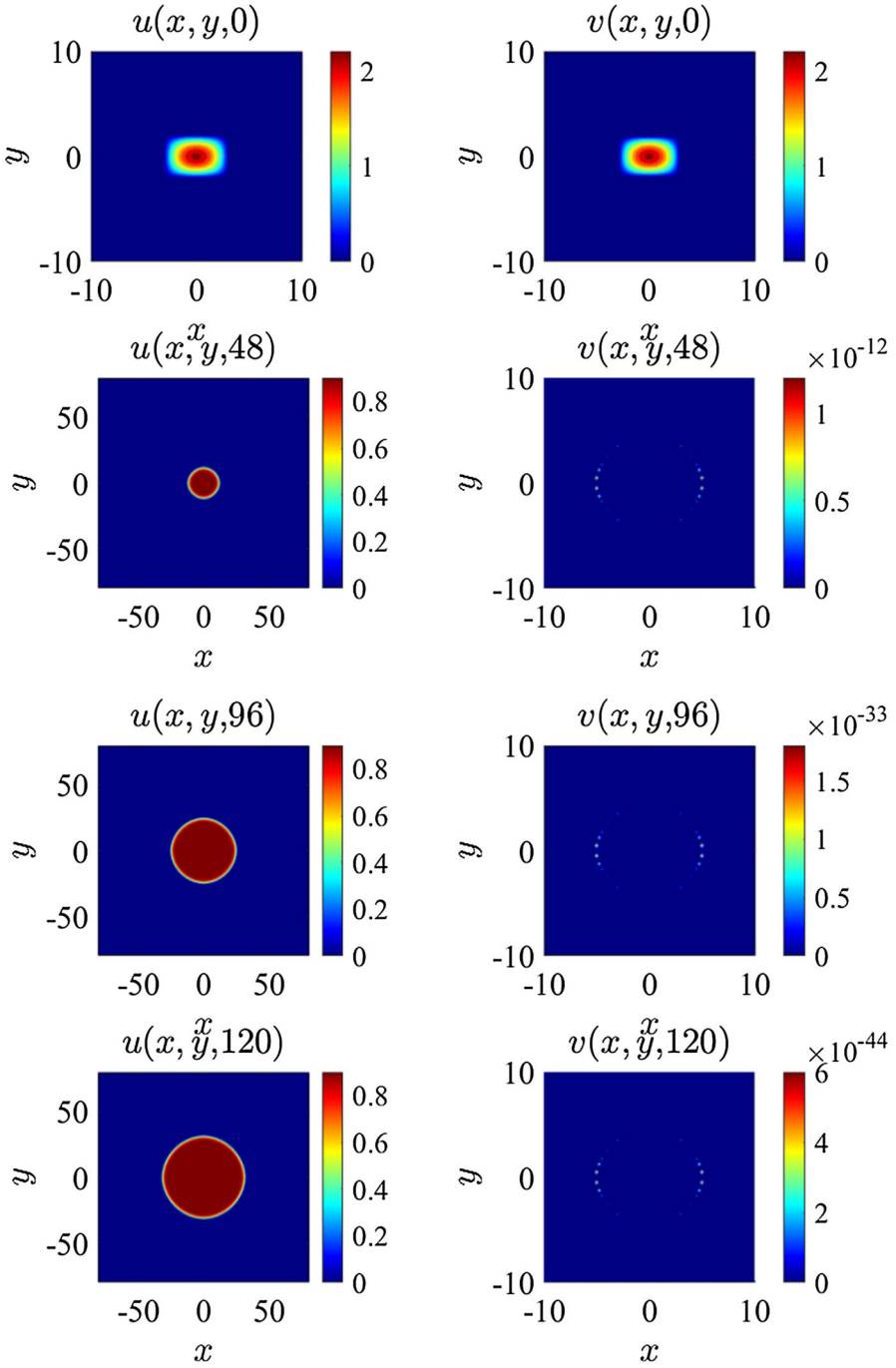

Fig. 49 Profiles of u and v with $(\lambda_1, \lambda_2) = (2.1, 2.0)$ at time $t = 0, 48, 96, 120$, exhibiting vanishing of v with u invading successfully. The profile of u becomes circular as time increases

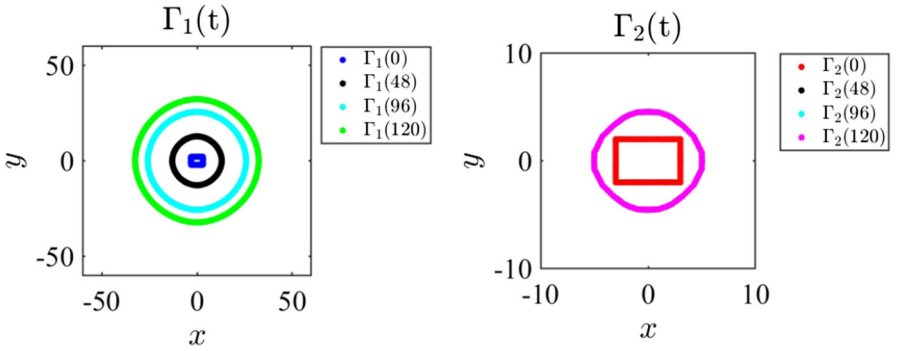

Fig. 50 Corresponding behaviour of $\Gamma_1(t)$ and $\Gamma_2(t)$ in Fig. 49 at time $t = 0, 48, 96, 120$. $\Gamma_1(t)$ becomes circular as time increases, while $\Gamma_2(t)$ barely moves after $t = 48$

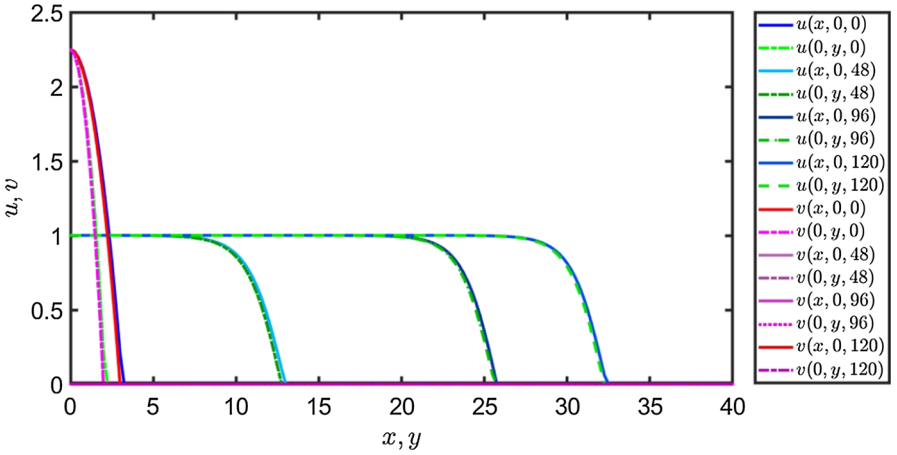

Fig. 51 Profiles of $u(x, 0, t)$, $u(0, y, t)$, $v(x, 0, t)$, $v(0, y, t)$ at $t = 0, 48, 96, 120$, obtained from the corresponding population distribution in Fig. 49, with u propagating like a traveling wave in both the x and y directions

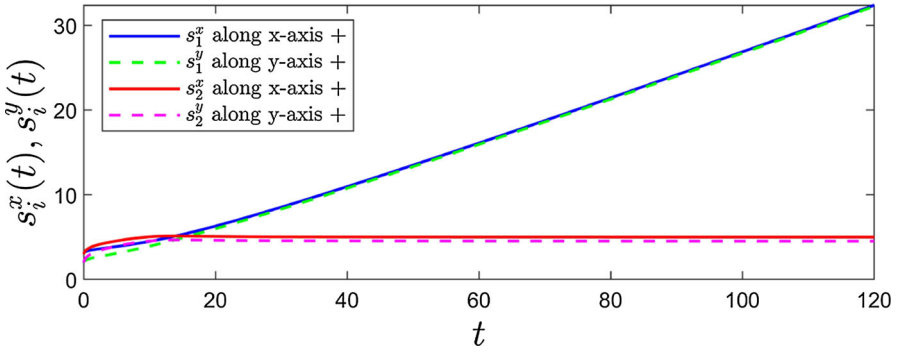

Fig. 52 The curves $s_i^x(t) := \Gamma_i(t) \cap \{y = 0\}$, $s_i^y(t) := \Gamma_i(t) \cap \{x = 0\}$ $(i = 1, 2)$ obtained from the corresponding moving boundaries in Fig. 50. $s_1^x(t)$ and $s_1^y(t)$ grow linearly, while $s_2^x(t)$ and $s_2^y(t)$ approach a constant as t increases

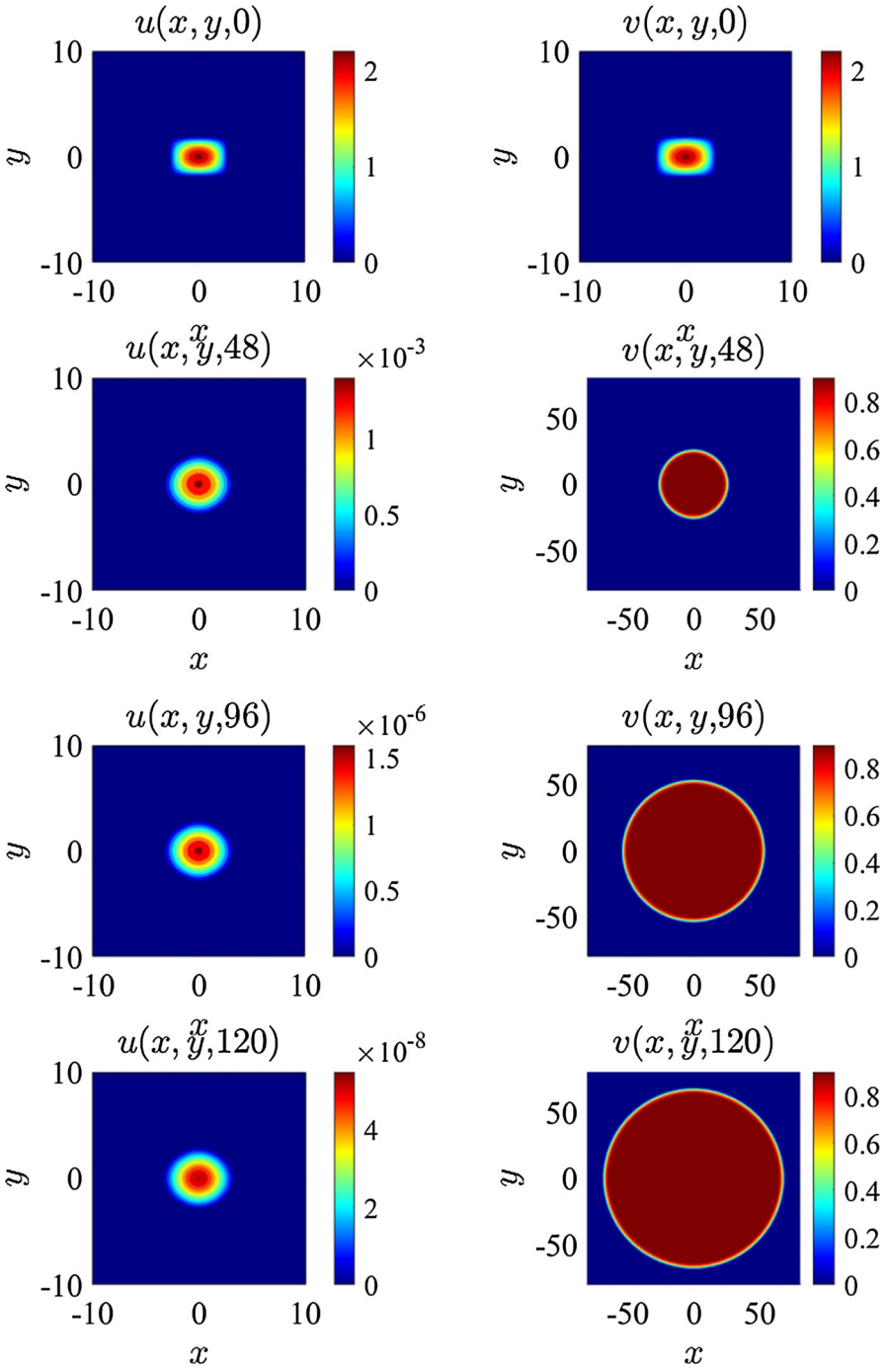

Fig. 53 Profile of u and v with $(\lambda_1, \lambda_2) = (1.9, 2.0)$ at time $t = 0, 48, 96, 120$, showing u vanishing and v invading successfully. The profile of v becomes circular as time increases

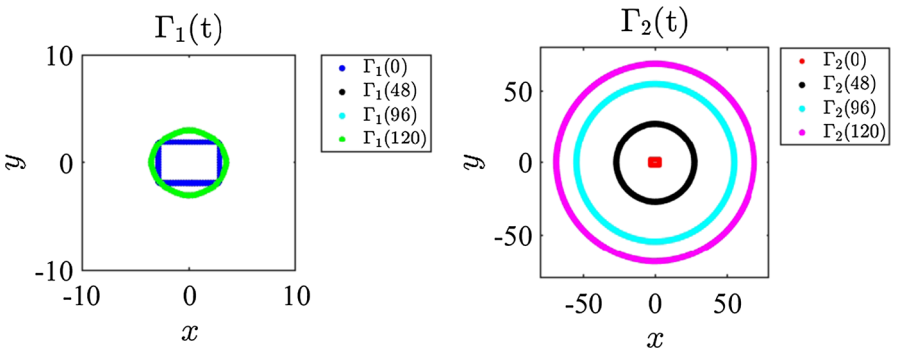

Fig. 54 Corresponding behaviour of $\Gamma_1(t)$ and $\Gamma_2(t)$ in Fig. 53 at time $t = 0, 48, 96, 120$. $\Gamma_2(t)$ becomes circular as time increases, and $\Gamma_1(t)$ barely moves from $t = 48$

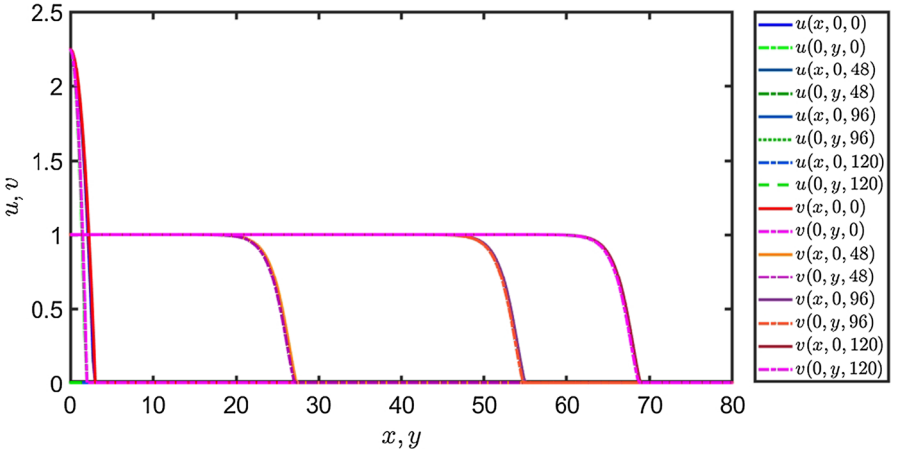

Fig. 55 Profiles of $u(x, 0, t)$, $u((0, y, t)$, $v(x, 0, t)$, $v((0, y, t)$ at $t = 0, 48, 96, 120$, obtained from the corresponding population distribution in Fig. 53, where v propagates like a traveling wave in both the x and y directions

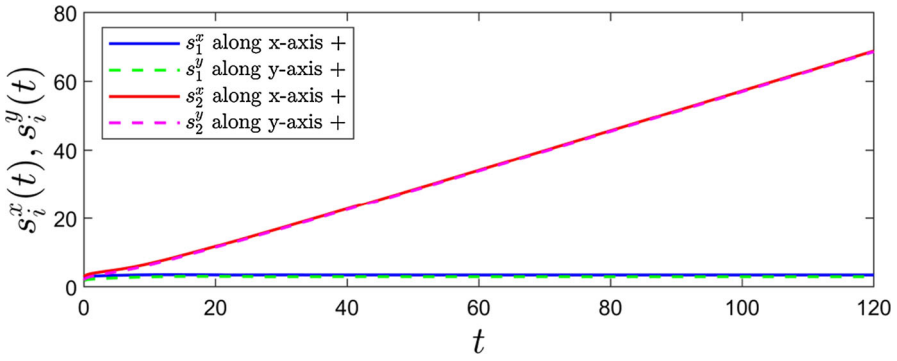

Fig. 56 The curves $s_i^x(t) := \Gamma_i(t) \cap \{y = 0\}$, $s_i^y(t) := \Gamma_i(t) \cap \{x = 0\}$ $(i = 1, 2)$ obtained from the corresponding moving boundaries in Fig. 54, where $s_2^x(t)$ and $s_2^y(t)$ grow linearly, while $s_1^x(t)$ and $s_1^y(t)$ approach a constant as t increases

This observation should be taken with care since there could be transition behavior which occur when the parameters (λ_1, λ_2) in the initial functions fall into some zero measure set of $\mathbb{R}^2$ (likely some curves, e.g., near the dotted lines in Fig. 11), which is difficult to observe through this kind of numerical experiments. Therefore it is likely that some of the transition behaviors are missing from this classification. Fortunately these possible transition behaviors hardly appear in the real world, though it is often of intriguing mathematical interest to determine them rigorously. Another limitation associated with the observation is that only some special types of initial functions are used in our numerical simulation, although we believe the findings in the observation are independent of the choice of the type of initial functions.

We would like to stress that for the 2D case without radial symmetry, no theoretical results are available so far for this model, though that is the most natural case for the model. We believe the classification of the longtime dynamical behaviors observed above for the 1D and 2D cases with radial symmetry should persist, at least when the initial population ranges are not in very strange geometrical shapes, which is supported by our numerical experiments in this paper. Moreover, for simpler single species models, theoretical results in Du et al. (2014) indicates that even though the initial population range may have an arbitrary shape, when spreading is successful, as time increases, the population range becomes more and more spherical. For two species models like the one under investigation here, no such theoretical result is known yet due to extra technical difficulties. Our numerical experiments with triangular and rectangular initial ranges suggest that such a property is retained by the two species competition model here.

The real environment in which invasive species compete and invade is never homogeneous, yet theoretical analysis of the model in heterogeneous environments becomes extremely difficult. Numerical analysis usually has a big advantage for such a situation, as the numerical methods which work effectively in the homogeneous case usually extend easily to the heterogeneous case. This is indeed the situation here. In view of daily and seasonal variations of the environment in the real world, time-periodic environment is a very natural and important case for consideration in mathematical modelling. For our model here, the competitive intensities and variations of reproductive activities of the species are naturally affected by seasonally fluctuating environment. We are particularly interested in knowing how these periodic fluctuations affect the spreading of the species. Our numerical analysis indicates that the basic features of the model are retained under such time-periodic perturbation of the environment, with the average spreading speed almost the same as in the case of homogeneous environment.

We hope the numerical observations here not only provide additional biological/ecological information which is lacking from existing theoretical work on the model, but also provide useful insights for further theoretical investigation. Moreover, we hope the numerical analysis here may inspire applications of some refined versions of the model tailored to concrete real world biological/ecological invasion problems.

References

Bunting G, Du Y, Krakowski K (2012) Spreading speed revisited: analysis of a free boundary model. Netw Heterog Med 7(4):583–603

de Mottoni P (1979) Qualitative analysis for some quasilinear parabolic systems. Inst Math Pol Acad Sci Zam 190:11–79

Du Y, Guo Z (2011) Spreading-vanishing dichotomy in a diffusive logistic model with a free boundary. II. J Differ Equ 250(12):4336–4366

Du Y, Guo Z (2012) The Stefan problem for the Fisher-KPP equation. J Differ Equ 253:996–1035

Du Y, Lin Z (2010) Spreading-vanishing dichotomy in the diffusive logistic model with a free boundary. SIAM J Math Anal 42(1):377–405

Du Y, Lin Z (2014) The diffusive competition model with a free boundary: invasion of a superior or inferior competitor. Discrete Contin Dyn Syst B 19(10):3105–3132

Du Y, Lou B (2015) Spreading and vanishing in nonlinear diffusion problems with free boundaries. J Eur Math Soc 17(10):2673–2724

Du Y, Matano H, Wang K (2014) Regularity and asymptotic behavior of nonlinear Stefan problems. Arch Rational Mech Anal 212:957–1010

Du Y, Matsuzawa H, Zhou M (2015) Sharp estimate of the spreading speed determined by nonlinear free boundary problems. SIAM J Math Anal 46:375–396

Du Y, Matsuzawa H, Zhou M (2015) Spreading speed and profile for nonlinear Stefan problems in high space dimensions. J Math Pures Appl 103:741–787

Du Y, Wang M, Zhou M (2017) Semi-wave and spreading speed for the diffusive competition model with a free boundary. J Math Pures Appl 107(3):253–287

Du Y, Wu C-H (2018) Spreading with two speeds and mass segregation in a diffusive competition system with free boundaries. Calc Var Partial Differ Equ 57(2):52

Fisher FA (1937) The wave of advance of advantageous genes. Ann Eugen 7:335–369

Girardin L, Lam KY (2019) Invasion of open space by two competitors: spreading properties of monostable two-species competition-diffusion systems. Proc Lond Math Soc 119:1279–1335

Guo J-S, Wu C-H (2012) On a free boundary problem for a two-species weak competition system. J Dyn Differ Equ 24(4):873–895

Guo J-S, Wu C-H (2015) Dynamics for a two-species competition-diffusion model with two free boundaries. Nonlinearity 28(1):1–27

Kearney M, Phillips BL, Tracy CR, Christian KA, Betts G, Porter WP (2008) Modelling species distributions without using species distributions: the cane toad in Australia under current and future climates. Ecography 31(4):423–434

Khan K, Liu S, Schaerf T, Du Y (2020) Invasive behaviour under competition based on a model with diffusion and free boundaries: A numerical approach, preprint (http://turing.une.edu.au/~ydu/papers/Comp-numerical.pdf)

Kolmogorov AN, Petrovski IG, Piskunov NS (1937) A study of the diffusion equation with increase in the amount of substance, and its application to a biological problem. Bull Mosc Univ Math Mech 1:1–25

Liu S, Du Y, Liu X (2020) Numerical studies of a class of reaction-diffusion equations with Stefan conditions. Int J Comput Math 97(5):959–979

Liu S, Liu X (2018) Numerical methods for a two-species competition-diffusion model with free boundaries. Mathematics 6(5):72

Liu S, Liu X (2020) Krylov implicit integration factor method for a class of stiff reaction-diffusion systems with moving boundaries. Disc Contin Dyn Syst B 25(1):141–159

Okubo A, Maini PK, Williamson MH, Murray JD (1989) On the spatial spread of the grey squirrel in Britain. Proc R Soc Lond B 238(1291):113–125

Piqueras M-A, Company R, Jódar L (2017) A front-fixing numerical method for a free boundary nonlinear diffusion logistic population model. J Comput Appl Math 309:473–481

Shine R (2014) A review of ecological interactions between native frogs and invasive cane toads in Australia. Austral Ecol 39(1):1–16

Tian C, Ruan S (2018) On an advection-reaction-diffusion competition system with double free boundaries modeling invasion and competition of Aedes albopictus and Aedes aegypti mosquitoes. J Differ Equ 265:4016–4051

Wang MX, Zhang Y (2017) Note on a two-species competition-diffusion model with two free boundaries. Nonl Anal 159:458–467

Wang Z, Nie H, Du Y (2019) Asymptotic spreading speed for the weak competition system with a free boundary. Discrete Contin Dyn Syst Ser A 39:5223–5262
Wu C-H (2013) Spreading speed and traveling waves for a two-species weak competition system with free boundary. Discrete Contin Dyn Syst Ser B 18(9):2441–2455
Wu C-H (2015) The minimal habitat size for spreading in a weak competition system with two free boundaries. J Differ Equ 259(3):873–897